SITELLE :
A PRIMER

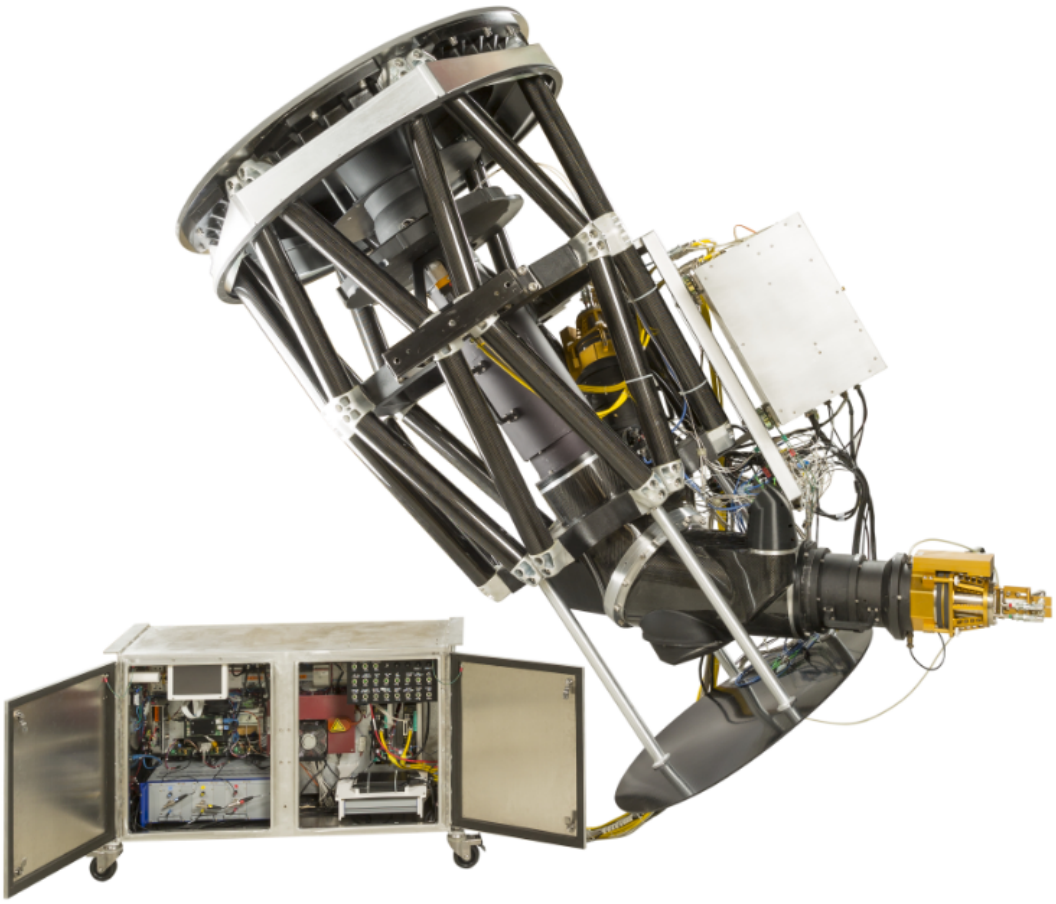

(Picture courtesy of ABB)

Laurent Drissen, Thomas Martin, Laurie Rousseau-Nepton, Alexandre Alarie, Julie Mandar, Antoine Bilodeau, Marc Baril, Sébastien Lavoie, Mike Tommy Duchesne, Frédéric Grandmont, …

Version 2.0 (January 2016)

Imaging Fourier Transform Spectroscopy: A Primer for SITELLE Users

SITELLE[1] is an imaging Fourier transform spectrometer (iFTS) - a Michelson interferometer-based IFU - aimed at obtaining spatially resolved spectra, in selected wavebands of the visible (350 - 900 nm), of extended sources in a 11 x 11 arcminute field of view. Spatial resolution is limited by the seeing (typically 0.8" at CFHT) and pixel size (0.32"). Spectral resolution is chosen by the user, from R ~ 1 (Deep image) up to R ~ 10 000, but is limited by the choice of wavelength range (filters) and object brightness.

The typical « niche » for SITELLE is the observation of extended objects (nebulae, galaxies, galaxy clusters) with emission lines, at R ~ 500 – 2500. Observations of objects with continuum and absorption lines (star clusters, elliptical galaxies) are also possible, but iFTS are not optimized for this (see section 5.2). Some examples of data obtained during SITELLE's commissioning and Science verification phases are described in section 7 (pp 26 - 45).

Raw SITELLE data consist of two sets of complementary interferometric images, as recorded by CCD cameras (2048 x 2048 pixels) located at each output port of the interferometer. The interferogram cube is built by obtaining a series of short exposures (typically 2s to 100s, depending on the target flux and required spectral resolution) obtained while moving, step-by-step, the Michelson interferometer's moving mirror. After data processing and calibration, the user obtains a data cube made of (2048 x 2048 0.32''-pixels in the spatial domain) x (a few hundred spectral resolution elements) – see *Figure 1*. The main technical characteristics of SITELLE are summarized in *Table 1*.

Table 1 – SITELLE characteristics

Field of view	**11' x 11'**
Detectors **Readout time** **Readout noise**	**2048^2 e2v** **3.2s** **5e**
Pixel size	**0.32''**
Wavelength range	**350 – 900 nm**
Spectral resolution	**1 – 10 000**
North & South limits (6-inch clearance)	**-38^o...$+67^o$**

[1] **S**pectromètre **I**mageur à **T**ransformée de Fourier pour l'**E**tude en **L**ong et en **L**arge de raies d'**E**mission.

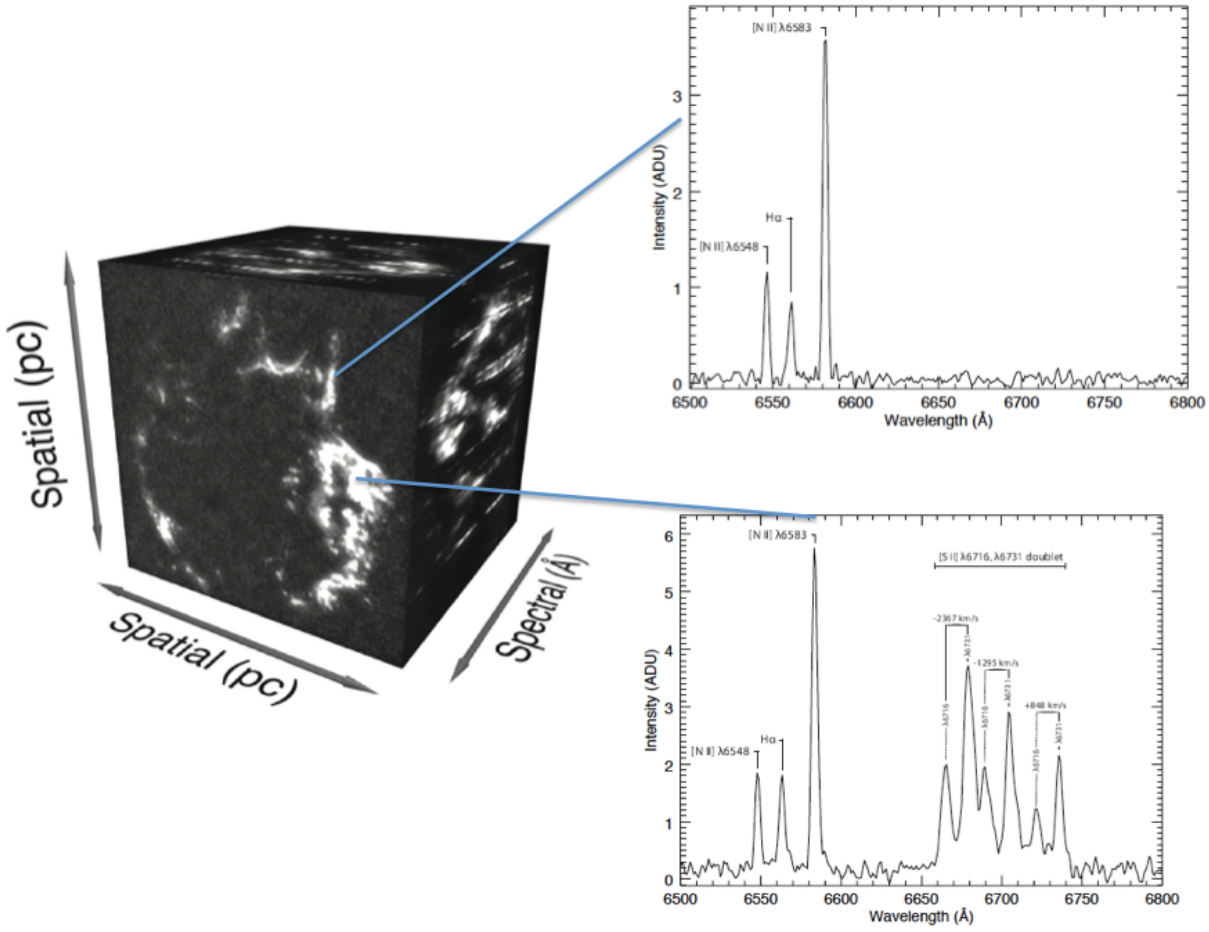

Figure 1 – A typical output from an iFTS. Data cube of the Cas A supernova remnant, obtained with SpIOMM. For each pixel on the detector, a spectrum (in this case, from 650 to 680 nm) can be extracted. Only the central 5' x 5' of the entire cube are shown. Adapted from Alarie et al. (2014; MNRAS 441, 2996).

SpIOMM, the prototype for SITELLE, has been used on a regular basis at the Observatoire du Mont-Mégantic. Data obtained with SpIOMM are shown throughout this document.

The objective of this document is to provide prospective users with enough information on the iFTS principle and SITELLE's performance to be able to plan and optimize an observing run. A data simulator is also available (http://www.cfht.hawaii.edu/Instruments/Sitelle/SITELLE_etc.php).

1 – The core of SITELLE : a Michelson interferometer

An astronomical iFTS is basically a Michelson interferometer inserted into the collimated beam of an astronomical camera system, equipped with two detectors. Spectra of every source of light in the field of view (11 arcminutes in the case of SITELLE) are acquired through a series of images obtained by moving one of the two mirrors of the interferometer, producing an interferometric data cube which is then Fourier transformed to produce a spectral data cube.

The iFTS is composed of :
* A collimator ;
* A filter wheel to select the appropriate bandpasses ;
* The Michelson interferometer - see *Figure 2* – which consists of :
    - A beamsplitter used to separate the incoming beam into two equal parts ;
    - Two mirrors on which the halves of the original beam are reflected back ;
    - A moving mechanism to adjust the position and orientation of one of the mirrors (the other mirror is fixed) ;
    - A metrology system (IR laser and detector) to monitor the mirror alignment ;
* Two output camera optics;
* Two CCD detectors.

All wavelengths from the field are simultaneously transmitted to either one or both of the interferometer outputs in which the array detectors sit. By moving one of its two mirrors, the interferometer thus configured therefore modulates the scene intensity between the two outputs instead of spectrally filtering it. This configuration results in a large light gathering power since no light is lost except through items common to any optical design: substrate transmission, coatings efficiency, and quantum efficiency of the detectors. All photons from the source can hence be recorded at each exposure provided that both complementary outputs of the interferometer are recorded. This requires a modification to the "standard" Michelson configuration in which half the light goes back to the source: the incoming light enters the interferometer at an angle allowing the two output beams to be physically separated (see *Section 3.1*). A CCD detector is then attached to each of the two output optic ports collecting the light from the interferometer.

While in most commercial FTSs targeting very bright sources the interferometer's mirror is moved at a regular, servoed speed, the weak signal from astronomical sources requires a stepscan approach. The interferogram cube is thus obtained through the acquisition of a series of short exposures (~10 s to ~2 minutes) with the two CCDs. Between each step, one of the two mirrors in the interferometer is moved by a very short distance (between 175 nm and ~5 μm, depending on the spectral resolution and waveband chosen – see below).

Because the core of SITELLE is a modified Michelson interferometer, let's start the primer with a short recap of the principle behind the Michelson.

Let's first make three assumptions (See *Figure 2*):
1 – The Michelson is in a standard configuration, with one of its output ports coinciding with the input beam; in this case, half of the light goes back to the source over the course of a cube.
2 - The source is perfectly monochromatic, a laser beam for instance;
3 - The detector is a single pixel photo-receptor.

We will later relax those assumptions to describe the "real thing".

At the beginning, the two mirrors of the interferometer are equidistant from the beamsplitter : Optical path 1 = Optical path 2. The light from the source first hits the beamsplitter. Half the light is reflected by the fixed mirror and comes back, while the other half is transmitted through

the beamsplitter, hits the moving mirror and is reflected back. The two beams then recombine and interfere at the beamsplitter.

Since the two optical paths are identical, the two beams are perfectly in phase with each other. This gives rise to a constructive interference: 100% of the incoming light reaches the detector. We take the first « mono-pixel image ». We then move the moving mirror by a fraction of a wave (wavelength of the incoming source of light). While the optical path to the fixed mirror stays the same, the optical path to the moving mirror is longer and when the two beams recombine they are slightly out of phase. The interference is not 100% constructive! A fair fraction of the light reaches the detector, the rest of it goes back to the source. We take the second image: the intensity is only a (fair) fraction of that of the first image.

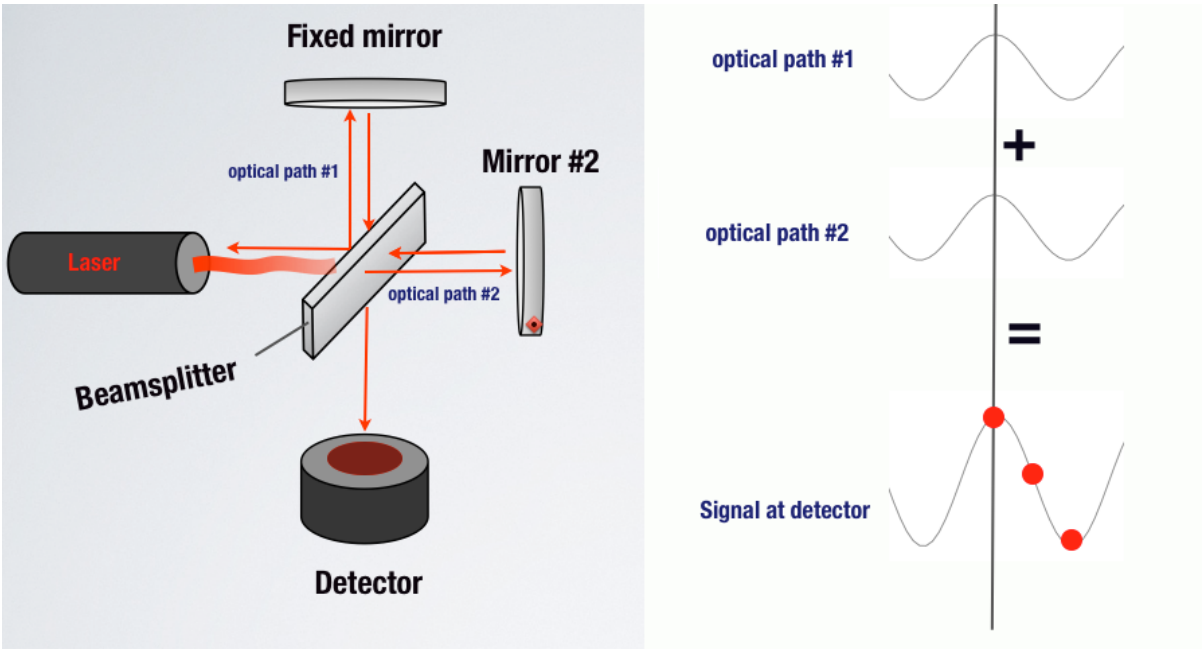

Figure 2 - A simple Michelson interferometer

We move mirror#2 a few steps farther until the two beams become completely out of phase. The interference is now completely destructive, so not a single photon reaches the detector: all of it goes back to the source and the third image is empty! [*We shall see in section 3.1 that, since we don't want light to escape back to the source, we modify this simple architecture to add a second detector in the system*].

We play this game many times in order to populate the interferogram of the source: a vector of intensities received by the detector as a function of the optical path difference (OPD) between the two arms of the interferometer.

If the source is monochromatic, the interferogram will have a sinusoidal shape (*Figure 2, lower right* panel; also *Figure 3, upper left* panel). The wavelength of this sine wave is directly related to that of the incoming light source. But if the source is polychromatic (in the sense of a few monochromatic sources), like an HII region, the signal at the detector as a function of step size

(or OPD) will be the sum of the interferograms of a series of monochromatic light sources (see *Figure 3, lower panel*).

How do we then deduce the spectrum of the incoming source? By analysing the interferogram with Fourier analysis. A Fourier transform of the interferogram provides the original spectrum of the source! Now, it makes sense to call SITELLE an imaging Fourier Transform Spectrometer, doesn't it?

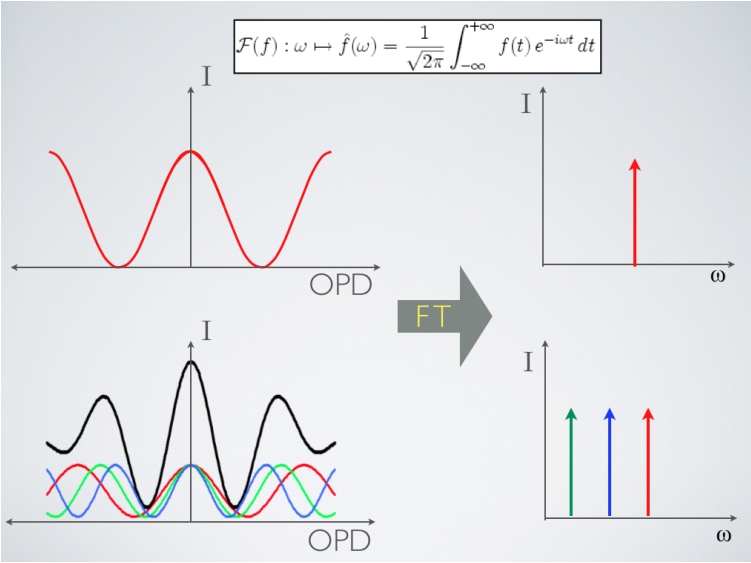

Figure 3 – Interferograms and their Fourier transform. A perfectly monochromatic source (upper panel) will give rise to a sine-wave interferogram pattern on the detector. Its Fourier transform is a delta function. A multichromatic light (three laser sources of different wavelengths, for instance; lower panel) produces a complex interferogram (black curve), which is the sum of the interferograms produced by its individual components. The Fourier transform of this pattern provides the frequencies of the original signal.

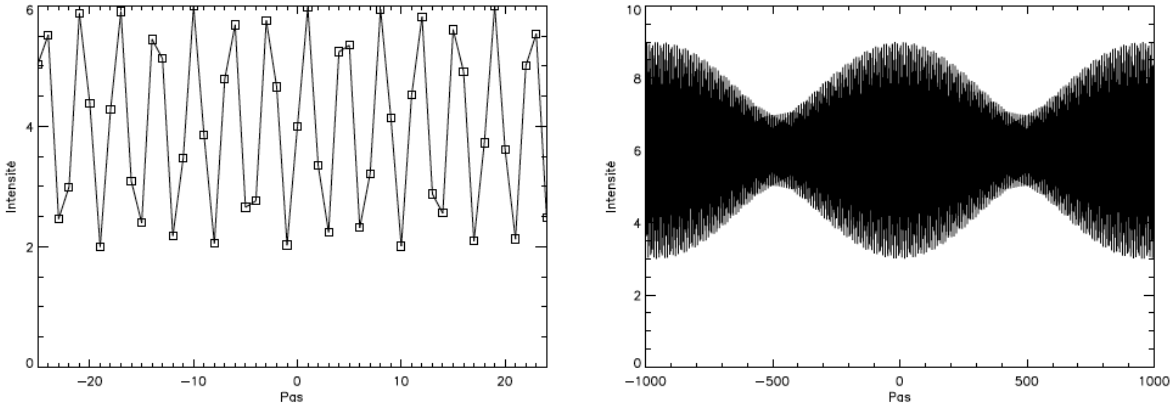

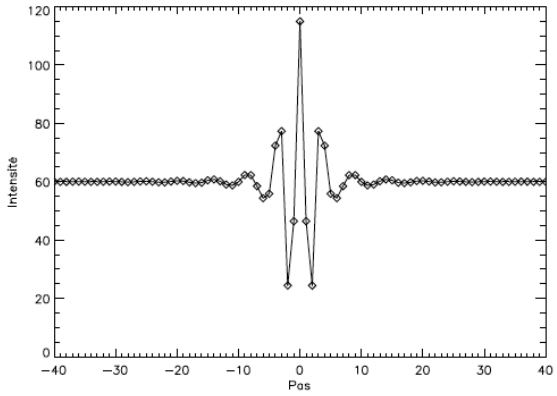

Figure 4 - Examples of simulated interferograms. From a single He-Ne laser (632 nm) on the upper left, a doublet (Hg 577 + 579 nm) on the upper right, and a continuum source on the lower panel.

2 - Spectral resolution, sampling and instrument line shape.

We just said that if the light source is monochromatic (a delta function), its interferogram is a perfect sine wave and then its Fourier transform is a delta function. But in real life, things are more complicated. Since we take an image at different discrete positions of the mirror, we do not sample the interferogram continuously. Then, it is logical to think that if we just take a few points in the interferogram, we will know the central wavelength of the emission line's peak with a poor precision; but if we increase the number of points away from the "Zero Path Difference" (ZPD), our precision will increase. This is also easy to show mathematically. It is even easier to figure this out if we assume that the source is a combination of two very close emission lines (like the Hg doublet at 577 & 579 nm - see *Figure 4, upper right* panel). Each line produces its own sine wave interferogram, with different (although very close to each other) periods. The resulting interferogram of this double signal is a sine wave modulated by a larger envelope : a classical « beating pattern ». If we only sample a small portion of it, we do not have the "big picture" and cannot resolve the doublet after Fourier transforming the interferogram. Sampling a larger portion increases the resolution: *in an FTS, spectral resolution is proportional to the maximum optical path difference between the ZPD and the last image of the data cube; this is illustrated in Figure 5* (simulation) and *Figure 6* (real data from SpIOMM).

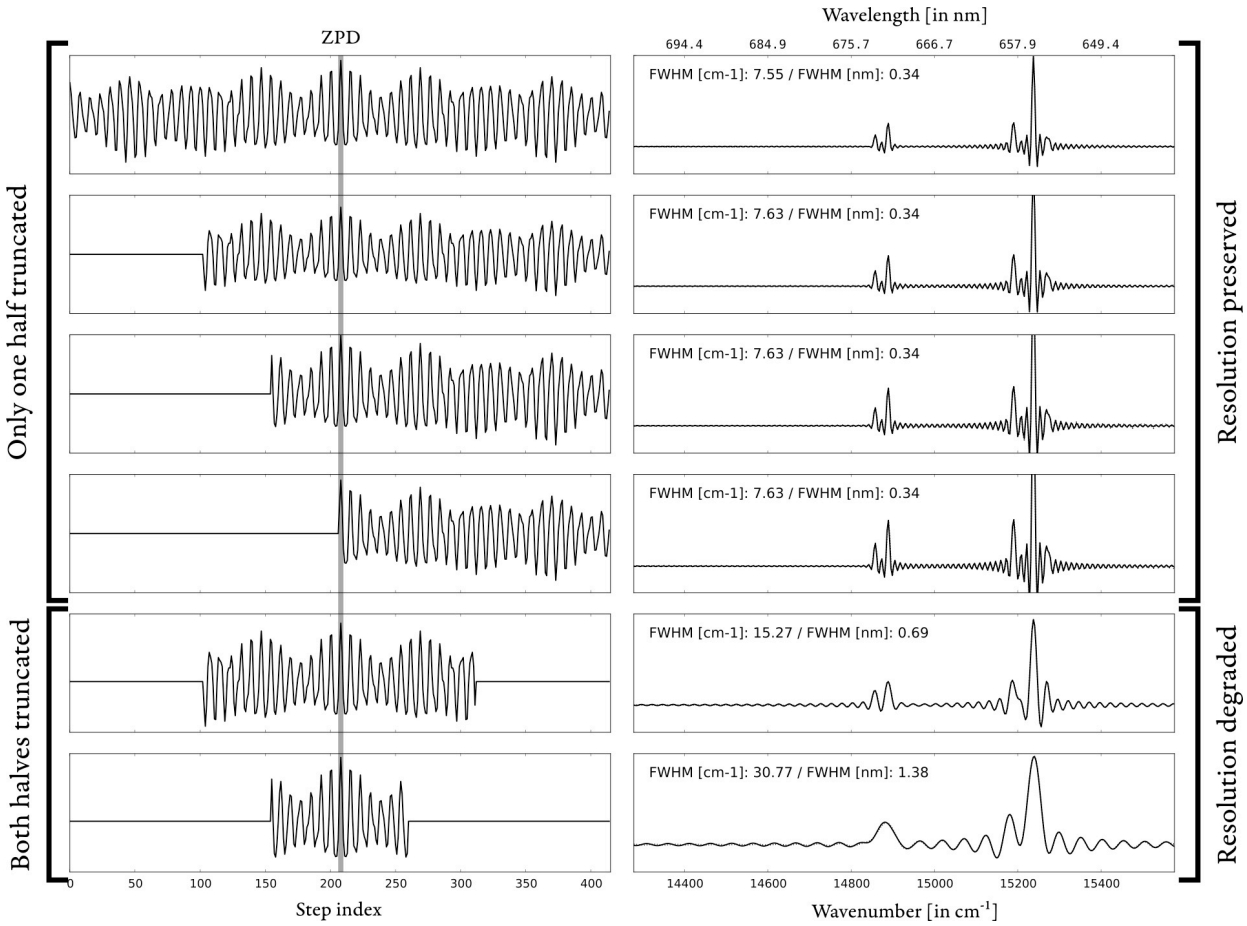

Figure 5 - Spectral resolution. Simulated interferograms (left) and their corresponding (unapodized) spectra showing that the spetral resolution is a function of the number of frames obtained on one side of the ZPD. The sidelobes, typical of an FTS Instrument line shape (see below), are obvious.

One cannot simply take an image at ZPD, move the mirror to a large OPD, take a second image and hope to get a very good spectral resolution: ***the interferogram has to be properly (Nyquist) sampled***. In practice, this means that the physical mirror step size should be smaller than half the shorter wavelength in the desired spectrum, if no spectral folding technique (see section 5.3) is used. A visible-band, unfolded (350 nm → ∞) spectrum thus requires mirror step sizes $\Delta x \leq 175$ nm.

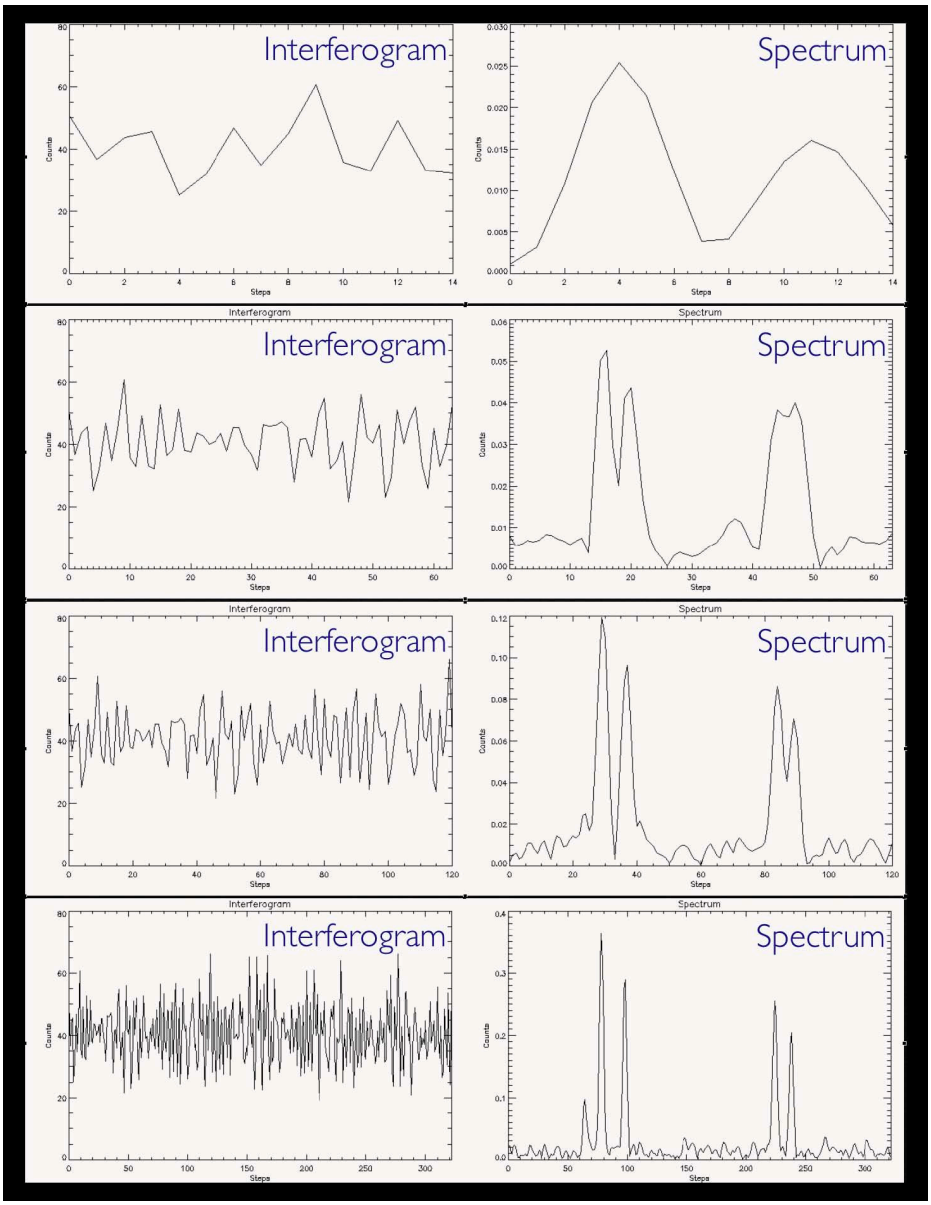

Figure 6 - Increasing spectral resolution as a function of total step number. On the left panels, we see the number of counts on a given CCD pixel at every step of the moving mirror (an interferogram). The Fourier transform of this signal is shown on the right panels. We see that after only a dozen steps, although the interferogram looks like noise, two groups of lines show up in the spectrum. As the number of steps increases, the interferogram takes a familiar « beating » shape and spectral resolution of its Fourier transform, the spectrum shown on the right panels, increases. The [NII] λλ6548, 6584, Hα and [SII] λλ6717, 6731 lines characteristic of supernova remnants are now well resolved. Taken from a red (650 – 680 nm) data cube of NGC 6992 (Alarie et al. 2014) with SpIOMM.

Finally, since we cannot spend an infinite time sampling the interferogram and the interferometer does not allow to scan an infinite OPD, our real signal is in fact a convolution of a discretely sampled sine wave with a boxcar function :

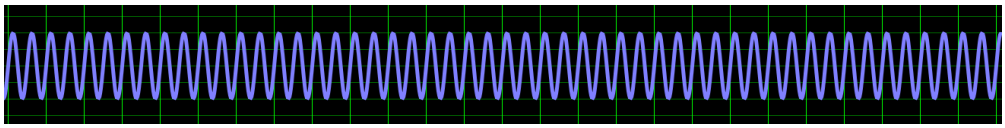

$f(x)$: infinite sinus-wave interferogram

$g(x)$: instrumental function

$$TF\left[f(x)\cdot g(x)\right]=\int_{-\infty}^{\infty} f(x)\cdot g(x)\,e^{-i\omega x}\,dx = F(\omega)\otimes G(\omega)$$

Assuming a perfect interferometer, the "instrumental function" is just a box representing the fact that the observations are finite in time (a few hours at most) and that the moving mirror's total displacement is limited. What is the Fourier transform of a boxcar function?

$$FI = TF\left[bc(x)\right]=\int_{-\infty}^{\infty} bc(x)e^{i\omega x}\,dx=\int_{-d}^{d} e^{i\omega x}\,dx=\frac{e^{i\omega x}}{i\omega}\Bigg|_{-d}^{d}$$

$$=\frac{1}{i\omega}\left[e^{i\omega d}-e^{-i\omega d}\right]=\frac{1}{i\omega}\left[\left\{\cos(\omega d)+i\sin(\omega d\right\}-\left\{\cos(\omega d)-i\sin(\omega d\right\}\right]$$

$$=2d\,\frac{\sin(\omega d)}{\omega d}$$

It's a sinc function! *Figures 7 & 8* below illustrate this. We will see in the next section that in processing the data we might want to damp the sidelobes to produce a more familiar, gaussian-like instrumental function; this process is called ***apodization***.

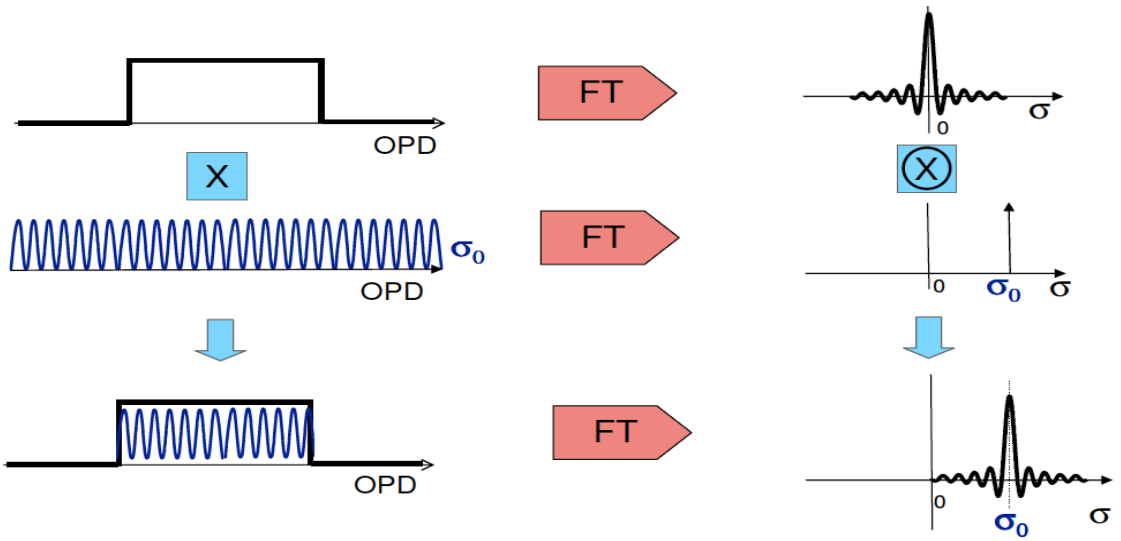

Figure 7 - Fourier transforms of a boxcar, an infinite sine wave, and the convolution of both.

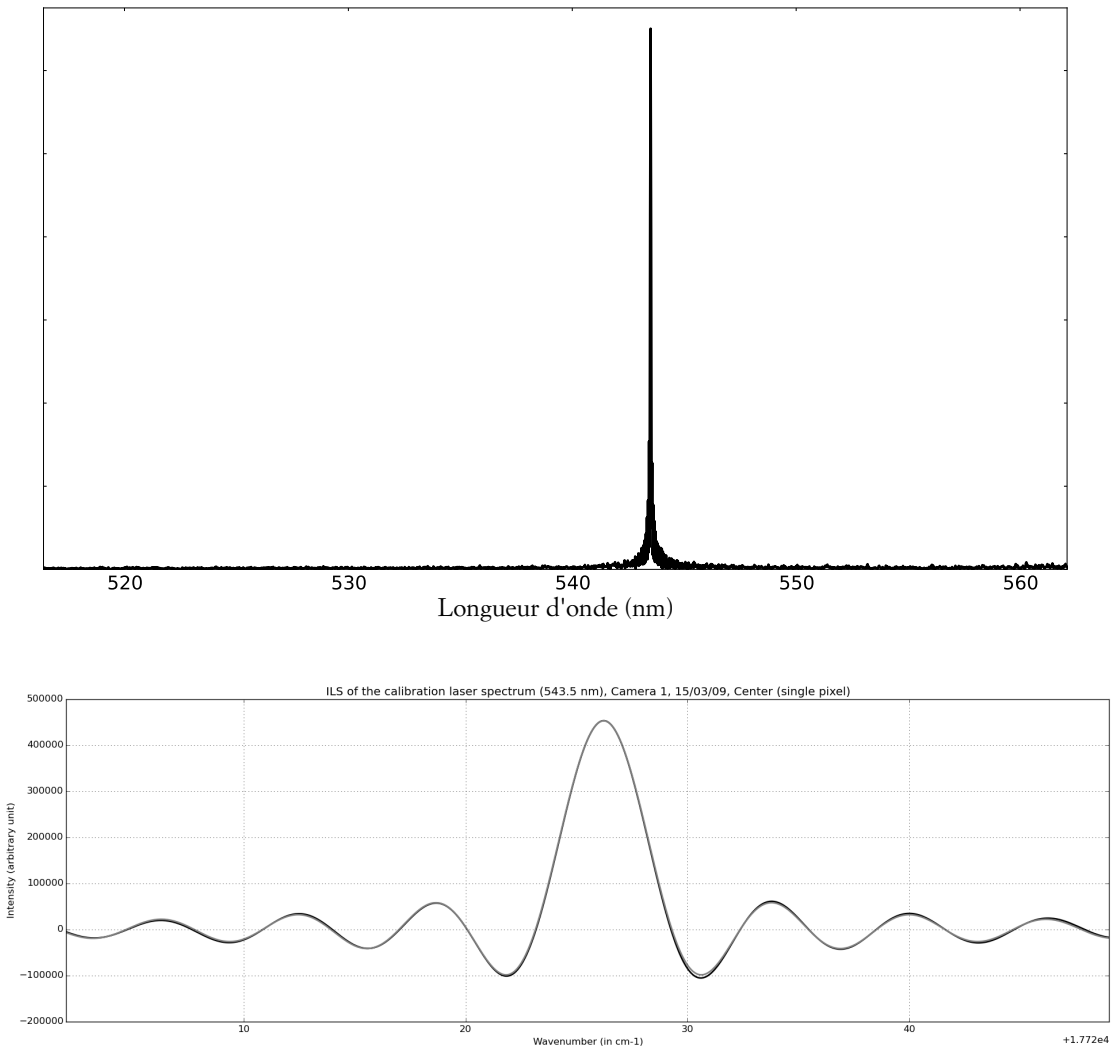

Figure 8 – Instrument line shape. The upper panel shows the instrument line function of the He-Ne calibration laser (543 nm) obtained by SITELLE in the laboratory. The enlargement (lower panel) shows the wings typical of a sinc function, characteristic of an FTS Instrumental line function. The dark curve is the real data whereas the lighter curve is a theoretical sinc function.

2.1 – Apodization

As one can see in *Figure 8* (and also *Figure 5*), the instrument line shape (ILS) looks a bit unusual to those of us familiar with the traditional slit spectrograph's roughly gaussian ILS. It consists of a main peak accompanied by a series of sidelobes of decreasing amplitudes as a function of distance from the main peak. These sidelobes should certainly not be considered as noise as they contain important information that is being taken into account by the data analysis software; indeed, ORCS (Section 6) does fit sinc functions on the unapodized data in order to maximise both the precision on line centers, line ratios and global SNR. It is however possible to attenuate the sidelobes in the spectra – to get a more familiar ILS, or a more nice-looking data cube - by convolving the interferograms with a proper function. This process, called apodization, is however done at the expense of a central peak's lower amplitude and increased fhwm. Apodization and its effects on the ILS are described in more detail by Norton & Beer (1976, Optical Society of America, 66, 259) and, more specifically to be used on Hershel/SPIRE-FTS data, by Naylor &

Tahic (2007, Journal of the Optical Society of America A, 24, 3644). *Figure 9* illustrates apodization on SpIOMM data.

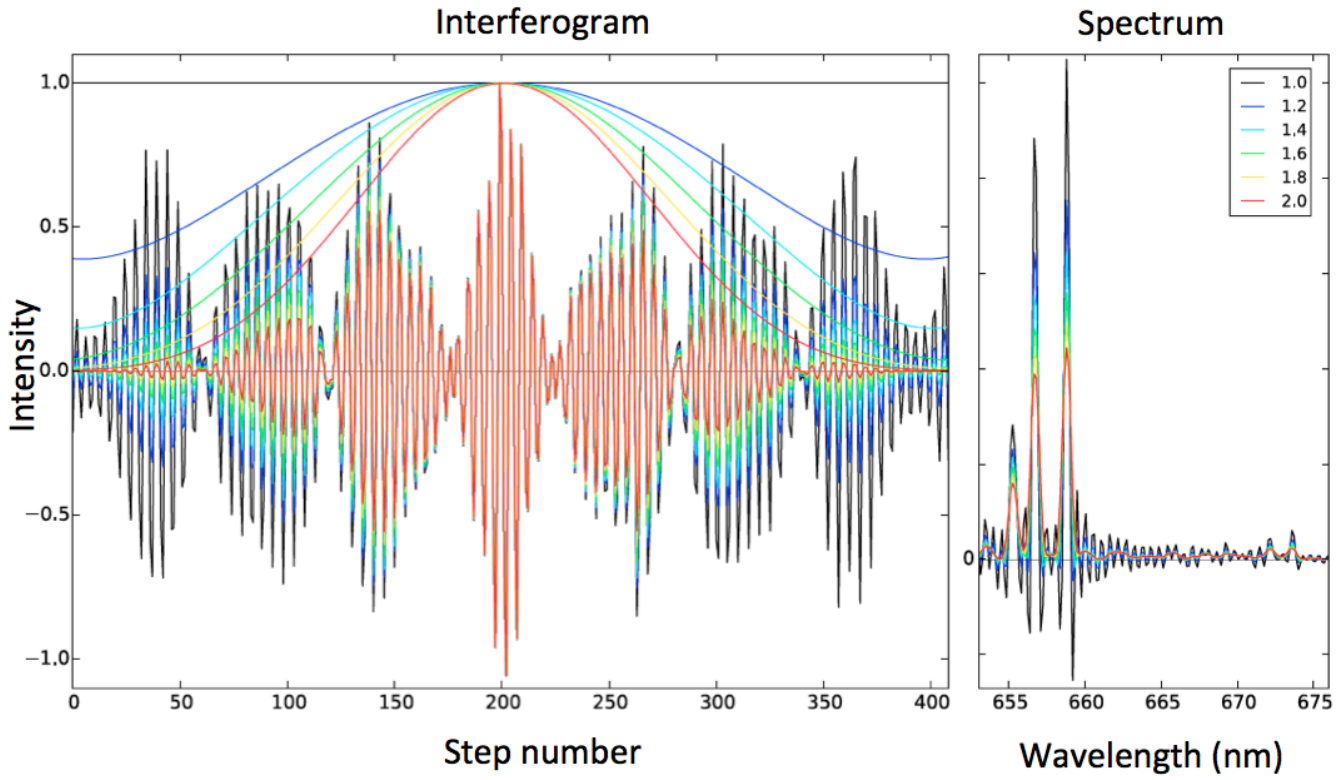

Figure 9 – Apodization. Effects of apodization on an interferogram of a nebula and its spectrum (M1-67 with SpIOMM), for different apodization strengths, from no apodization (1.0 – and thus a pure sinc function) to a strong one (2.0 – ILS is almost a pure gaussian). Adapted from T. Martin's Ph. D. thesis.

3 – From a classical FTS to a two-port imaging FTS : the real SITELLE.

The example described above is quite simple : a point-like source observed with a classical Michelson and a single single-pixel detector (see for instance Ridgway et al 1984, ApJS, 54, 177, for examples of stellar spectra obtained with KPNO's FTS in the late 1970's). Let's complicate things a bit to get closer to the real iFTS.

3.1 - Modify the Michelson

We said earlier that in a classical Michelson, a fraction of the incoming light goes back to the source. Although this is acceptable when the experiment is done in the lab, where the source is a powerful laser beam, this is clearly not a good option with astronomical sources. We want to keep all photons inside the instrument and eventually capture it in a detector. Not only do we collect more photons this way, but by collecting the sum of the two output ports we can disentangle the flux variations caused by the interference from those caused by varrying atmospheric extinction. Indeed, if the source is constant in time (no clouds), the sum of the two channels should not vary as a function of the step number : when one channel gets more flux, the other one gets less. Any fluctuation in the *sum of the two channels* can then be attributed to varrying absorption and hence corrected; we assume here that the sources are not intrinsically variable, at least on timescales comparable to the extent of a single datacube.

This is why in SITELLE, the incoming light enters the interferometer with an angle, which allows the "returning beam" to be physically separated from the incoming one. We just have to add a second detector there and voilà! See *Figures 10 & 11*.

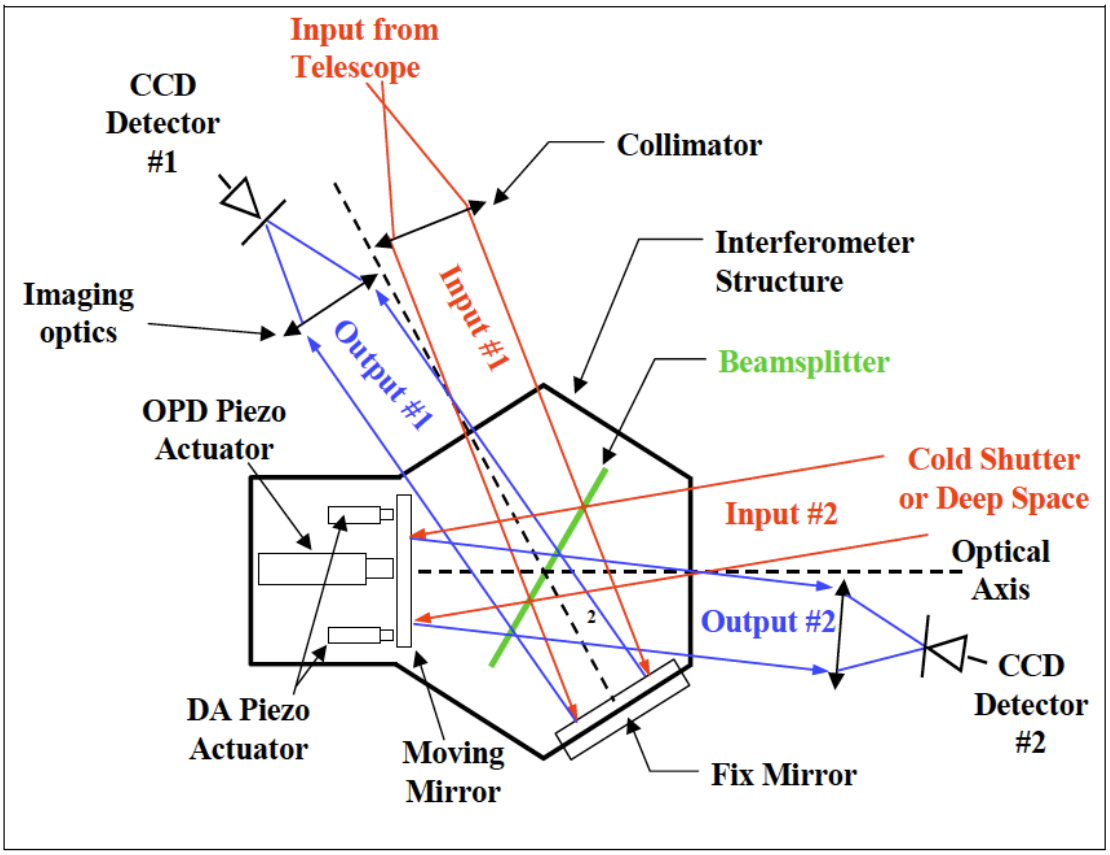

Figure 10 – Schematic view of SITELLE's interferometer

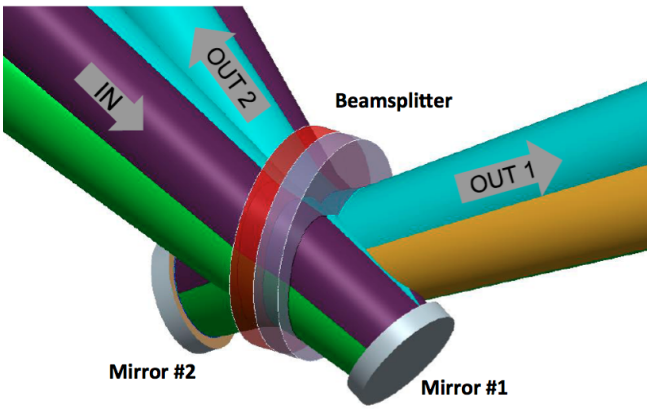

Figure 11 – Schematic view of SITELLE's beamsplitter/mirrors optical path

3b - Imaging optics and detectors

Second, we are not quite content with a single pixel detector since we want to obtain spatially sampled spectra of extended sources. To do this, we have two things to do. First, we add typical imaging optics to our aparatus: a collimator and a camera, each composed of multiple lenses (see Appendix B, where the optical design is described). Second, we replace the single pixel detector by a full frame CCD. In the case of SITELLE, we are using a 2k x 2k e2v CCD (See Appendix A). We have then modified the original Michelson into a fully functional dual-output imaging FTS!

3c - The beamsplitter

The beamsplitter is a critical component of SITELLE. Its optical quality and performance in terms of reflectivity/transmissivity over the entire visible bandpass dictate the FTS global performance, especially for the modulation efficiency (see section 4). SITELLE's beamsplitter *(Figure 12)* has been manufactured by Zygo Corporation, and is probably one of the finest ever designed and built.

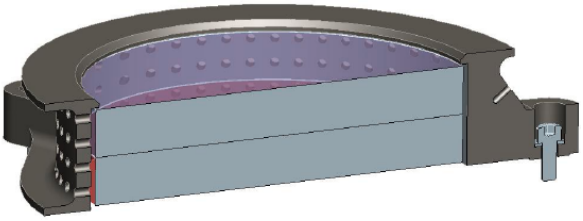

Figure 12 – SITELLE's beamsplitter.

4 - Modulation efficiency

Even if a good transmission is achieved in the optical design, contributing positively to the image's signal-to-noise ratio, it does not necessarily translate in a good performance for spectroscopy. In order to perform well on this aspect, a good modulation efficiency is also required. The performance of an FTS is thus characterized by its modulation efficiency (ME), i.e. the capability of the interferometer to modulate the incident light:

This parameter can be viewed as an analog to the grating efficiency in dispersive spectrographs. In the worst case scenario, where the modulation efficiency is zero, the light from the source is recorded on the detector but the interferogram is a straight line and no spectral information can be extracted from it (*Figure 13*). Details on the factors that affect SITELLE's ME are provided in Appendix D.

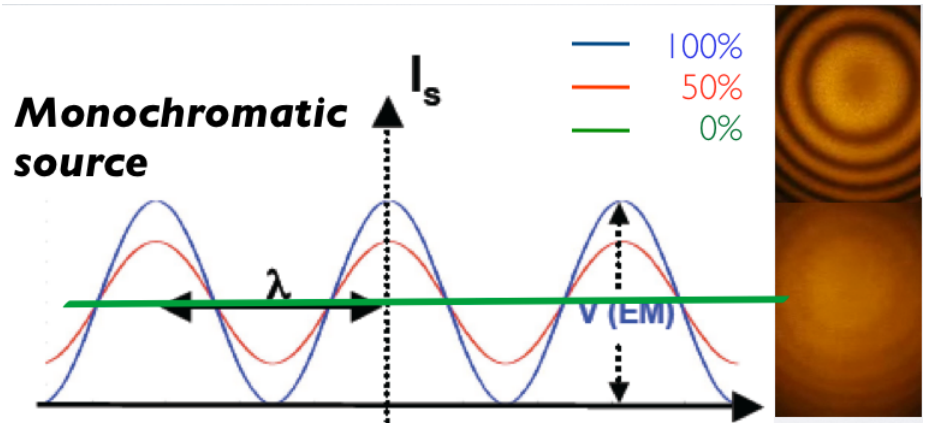

Figure 13 – Effect of modulation efficiency amplitude on an interferogram (left) and on fringe contrast (good ME, upper right; bad ME, lower right).

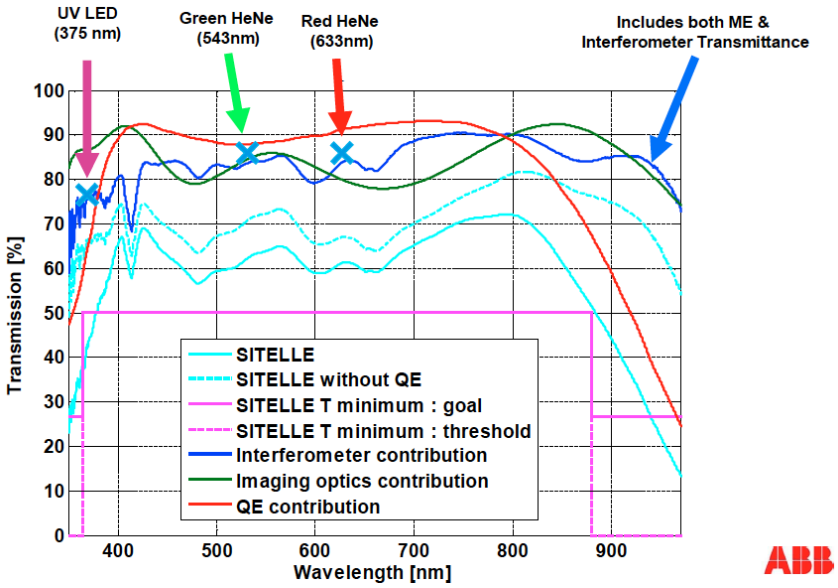

Figure 14 – SITELLE's expected modulation efficiency (goal and threshold) and measured values at three wavelengths (375 nm, 543 nm and 633 nm).

5 - Data acquisition, calibration, spectral resolution

5.1 – Data acquisition

The interferogram cube is obtained through the acquisition of a series of short exposure images with the two CCDs. Between two images, one of the two mirrors in the interferometer is moved by a very short distance (between 175 nm and ~ 5 µm, depending on the spectral resolution and waveband chosen). The signal at each pixel is modulated by a pattern which depends on the spectral content of the source (see *Figure 4*). The sum of the two images acquired at each step by the two detectors is similar to a single image obtained with a "normal" camera. Typical exposure times for each step vary between 15 seconds and 2 minutes, and the total number of exposures (mirror steps) between 100 and 1000, depending on the source brightness, filter bandwith and required spectral resolution – see also *Section 5.3*. The deadtime between two exposures is ~ 2 – 3 seconds (CCD readout & mirror movement and stabilization – see Appendix X), so the overheads represent about 2 – 20% of the total on-sky data acquisition. *Figures 15 – 17* illustrate the data acquisition process.

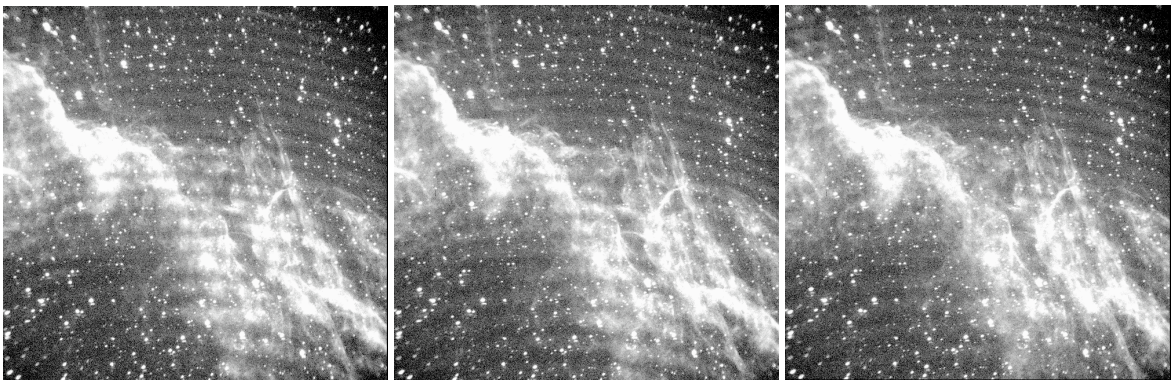

Figure 15- Series of images from a raw data cube - (one camera). The target is NGC 6992 (Cygnus Loop), obtained with a 650 - 680 nm filter. Notice the fringes, moving from one frame to the next; they are caused by a combination of night sky (OH) and nebular (Hα, [NII], [SII]) emission lines.

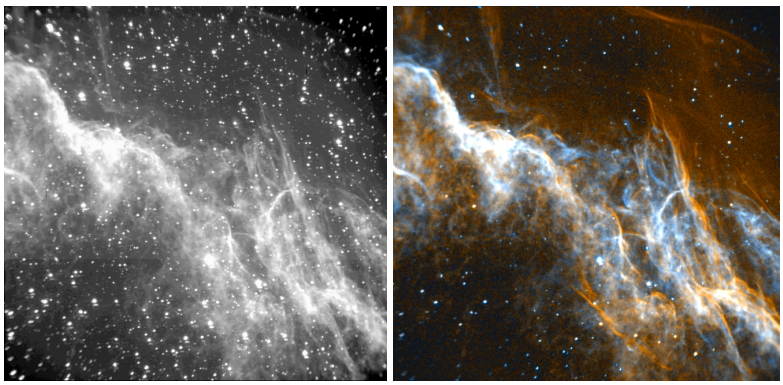

Figure 16- Sum and color-coded images. Images from the raw data cube can be co-added (left panel) to provide a deep, panchromatic image (within the limts of the filter). The image on the right is obtained

after Fourier transforming the original data cube and extraction of the Hα (red) and [NII] 6584 (blue) images.

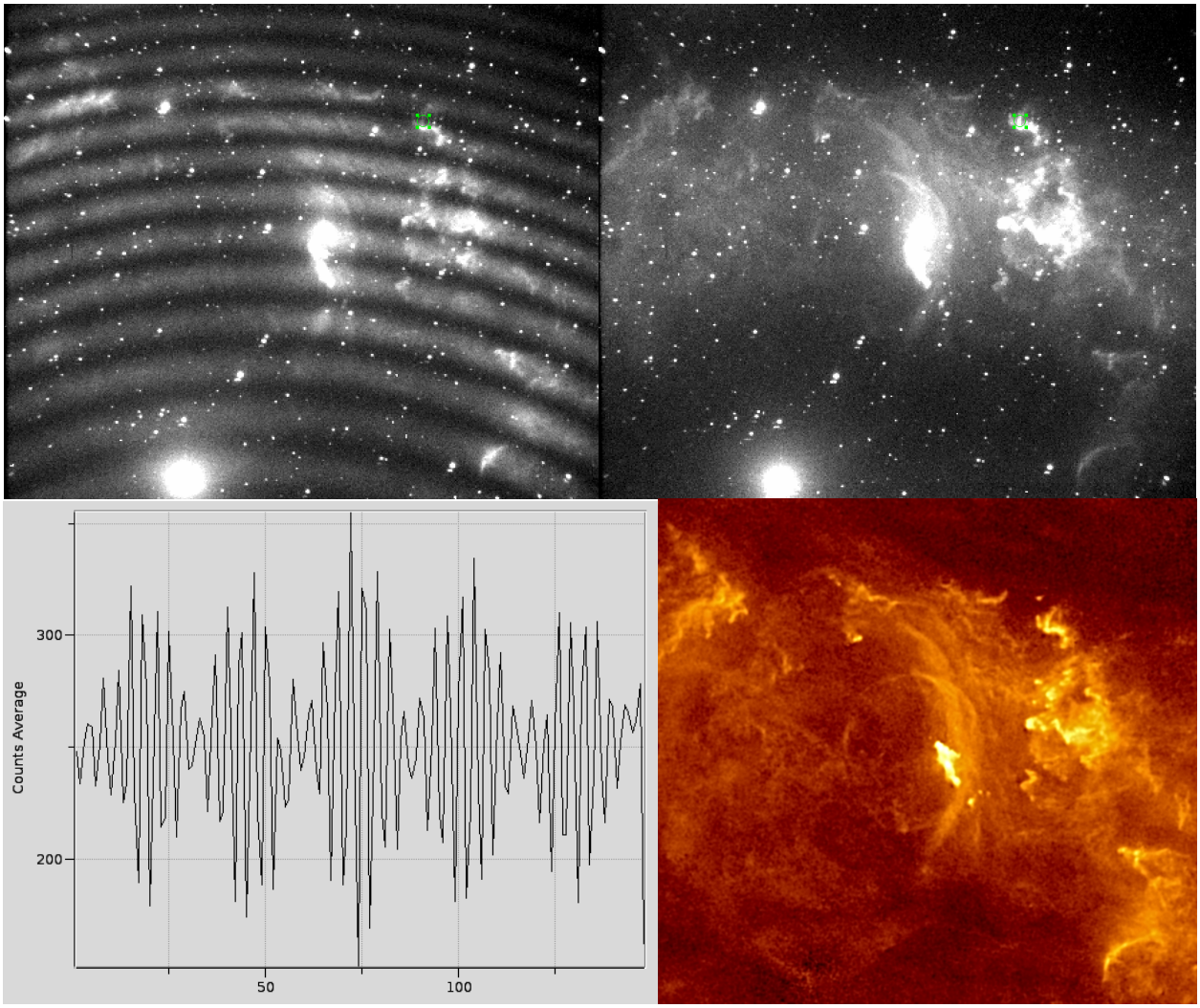

Figure 17 - Fringe spacing and OPD from SpIOMM data. Images from a raw data cube at two OPD positions (upper pannels - only one of the two cameras is shown), interferogram of a small region (lower left), and reduced image (lower right). The upper left image corresponds to step 18. It is far from the ZPD, so the fringes are close to each other. The upper right one corresponds to step 72, very close to the ZPD; only one constructive interference fringe is visible. Note that the center of the circular fringe pattern is outside the CCD because of the off-axis geometry of the interferometer (*Figure 10*). This data cube was obtained with a narrow filter centered on the [SII] 6716, 31 doublet : two nearby emission lines of almost equal intensity give rise to a distinct beating pattern in the interferogram (see simulated interferogram of Hg doublet in *Figure 4*). At some OPDs (see steps ~ 1, 30, 60, 80 and 118 in the interferogram, for instance), the fringe contrast is very low, not because the modulation efficiency is low but rather because the two emission lines interfere destructively at these phases. The target is NGC 7635 and its surroundings. The lower right image results from the extraction of the [SII] wavelengths out of the Fourier-transformed cube – continuum has been subtracted.

Images on *Figures 15 and 17* clearly show interference fringes because the field of view is covered with emission line sources : extended nebulae and night sky OH lines – red cubes of spiral galaxies also show these obvious fringes : the interferogram cubes « speak for

themselves ». This is very useful during a cube acquisition to make sure that the interferometer is working properly. However, this kind of fringe will not be obvious on continuum sources (stars, elliptical galaxies) nor in data obtained with filters excluding night sky lines (mostly in the blue), except close to the ZPD, where the flux will dramatically oscillate between the two cameras (see lower panel of *Figure 4*, and *Figure 18*). Interferometric data cubes of fields including many, almost point-like emission-line sources (clusters of galaxies with [OII] emission, for instance), will also be difficult to gauge at first sight. Only close scrutiny of the small targets in the interferogram or the Fourier-transformed cubes will tell us about their spectral content.

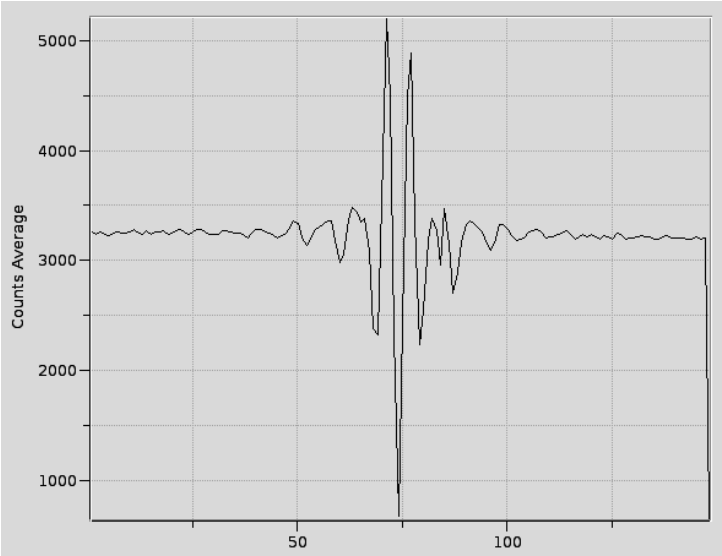

Figure 18 – Interferogram of a star in the same cube as Figure 17. Contrary to the nebular interferogram shown in *Figure 17*, this one shows clear oscillations only in the central third of the cube, close to the ZPD (step 74). Another cube of the same star obtained with a wider filter would show clear oscillations on an even smaller portion of the interferogram. Compare with the simulated spectrogram in the lower panel of *Figure 4*.

5.1 - Calibrations

Data cubes from an imaging FTS are obtained with a CCD, so all calibration data usually obtained with an imager are also required for SITELLE : dark, bias and flatfield frames for image detrends, images of standard stars for flux calibration. But since the purpose of an FTS is to obtain spectral information on the targets, typical calibration spectra are also obtained. The first « unconventional » calibration to be obtained (usually once at the beginning of each run) is a laser data cube. SITELLE is equipped with an internal integration sphere and a 543 nm laser source. On SpIOMM, a He-Ne (632.82 nm) laser is used. Because of the off-axis structure of the interferometer, the optical path is different for each element of the field of view on the CCD (see *Figure 10*) and the FFT of the signal will be centered on a different wavelength for each pixel. The laser cube is thus used to determine the wavelength correction to be applied to each pixel on the CCD (*Figure 19*). This calibration process is the equivalent of obtaining a Cu-Ar arc spectrum on a multi-slit spectrograph.

Spectrophotometric standard stars are also observed : once or twice during a run, a low-resolution data cube is obtained and images of standards can be obtained during each night. Our experience with SpIOMM has shown that the absolute wavelength calibration is not always very

precise (0.1 nm), but this is mostly due to flexure in the instrument : the calibration datacube is always obtained at zenith, while the science data are gathered at different zenith distances.

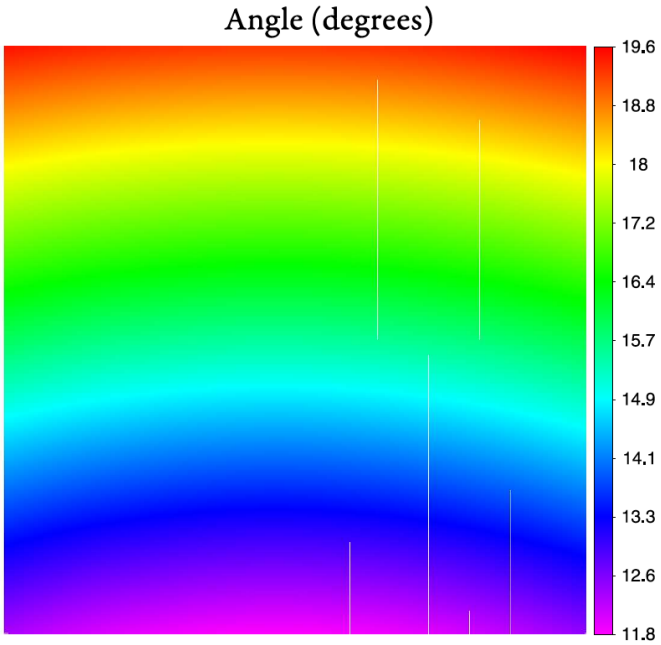

Figure 19 – Off-axis angle in the interferometer at each pixel. This angle was determined from the central wavelength of a HeNe (543 nm) laser as measured in SITELLE with a high resolution data cube; it varies between 11.8º and 19.6º. The « observed » wavelength of the laser thus varies between ~555 nm (543 nm / cos[11.8]) and ~576 nm (543 nm / cos[19.6]).

Night sky emission lines (Essentially OH lines in the red) can also be used for wavelength calibration. Precision of ~ 1 km/s on radial velocities have regularly been obtained on galactic nebulae. SITELLE is much stiffer than SpIOMM and we expect a much higher precision on the wavelength zero-point.

5.2 - Distributed noise and sky background

Although the iFTS has clear advantages over other integral field spectrographs, an obvious disadvantage is the *distributed photon noise*. Whereas the photon noise on a given pixel at a given wavelength in a spectrogram obtained with a dispersive element is only caused by photons at that particular wavelength, the case is very different with an FTS : at every step of the moving mirror, all photons from the entire bandpass are collected by that same pixel. The Fourier transform will then distribute this photon noise over all wavelength bins. The high troughput of the iFTS, combined with its distributed noise property, is the reason why this kind of instrument is so efficient to detect and characterize emission-line objects but lose their edge over dispersive spectrographs when continuum and absorption line sources are targetted (see Bennett 2000, ASP Conf. 195, p.58; and Maillard et al. 2013, Exp. Astr. 35, 527). Nevertheless, stellar spectra have been obtained in the past with single-pixel FTS (see Ridgway et al. 1984, ApJS, 54, 177 for exquisite high-resolution IR spectral of cool stars) and we have also demonstrated that SpIOMM is capable of obtaining spectra of continuum sources with absorption lines (*Figure 20*).

Because of the distributed noise, when dealing with very faint sources it is fair to say that « the sky is the limit », even for emission-line objects. In these cases, the background sky is the main source of photon noise; this has two consequences : observing faint targets with the Moon up is not a good idea (*Figure 21*), and observing them in the red ($\lambda > 700$ nm), where the night sky continuum and the large numbers of OH lines brighten the background even in moonless nights, is more difficult than in the blue-green region. This is also true for any imagery, but dispersive spectroscopy allows a dilution of the night sky contribution whereas FTS does not. Whereas an excellent mean night sky spectrum can be obtained and subtracted from the source's spectrum, as with long-slit spectroscopy, photon noise from the sky cannot be removed. This is where Mauna Kea has a net advantage over all other places, since it has the darkest sky, auroral emission is minimal, and even the Moon light is minimized when the transparency is excellent.

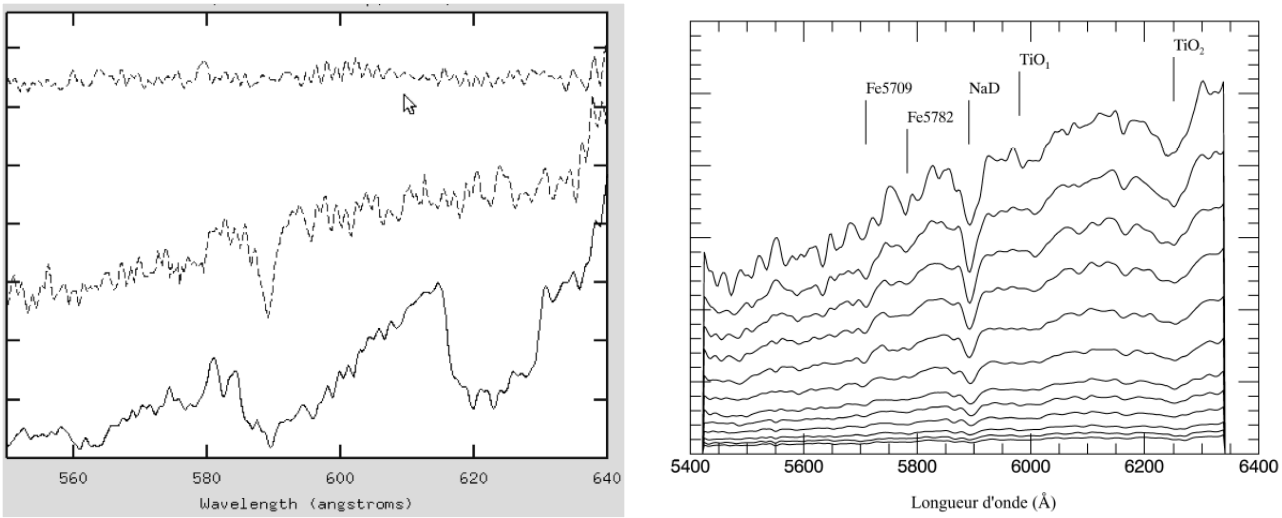

Figure 20 – Spectra of absorption line source with SpIOMM. On the left, individual stars (v ~ 14.5) in the field of the planetary nebula M27 : from top to bottom, the central white dwarf with a featureless spectrum, a G dwarf with the NaD line, and an M star with prominent TiO bands. On the right panel, a series of spectra (summ of pixel in annuli from the core to the outskirts) of the giant elliptical galaxy M87, where TiO bands, NaD and Fe lines are clearly visible.

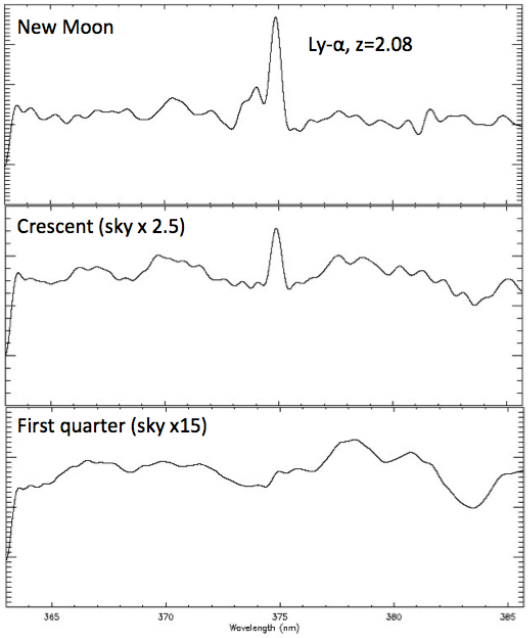

Figure 21 – Effect of the sky brightness on the detectability of a faint emission line. Simulated spectra of a faint Lyman-α line, R=1000, with different sky backgrounds. The effect of the Moon is obvious.

A filter in the green (C2: 559 – 625 nm) has been especially designed to avoid the bright [OI] 557.7nm and 630.0 nm sky lines. This is then a good moment to introduce the need for filters when observing with SITELLE, the subject of the next section.

5.3 - Filters and spectral folding

When observing with an FTS, compromising between spectral resolution and spectral coverage is of the essence. Although the data are not obtained by « scanning » the bandwidth of interest one wavelength element at a time, a proper sampling of the interferogram requires a minimum of mirror steps for a given bandwidth/resolution combination (see *Figure 22*). Remember that increasing the spectral resolution is obtained by moving the mirror to larger distances (OPDs) from the ZPD with a step size satisfying the Nyquist sampling period.

It is however possible to « cheat » and sample the total OPD with step sizes which are multiple (*m*) of the Nyquist period in order to obtain the desired spectral resolution in a given bandwidth (say, 600 – 700 nm). In this case however, the signal is « folded » onto itself : if a signal (sky background, continuum or emission lines from the source) is present outside of the bandwidth, it will be superimposed *m* times on the spectral region we want to analyse, which is not a good idea.

The obvious way around this problem is to use a filter which prevents photons outside the desired bandwidth to interfere into the folding process, thus allowing to increase the spectral resolution inside the filter limits while increasing the step size and thus decrease the number of steps.

The second reason to use filters is to reduce the distributed photon noise (see above).

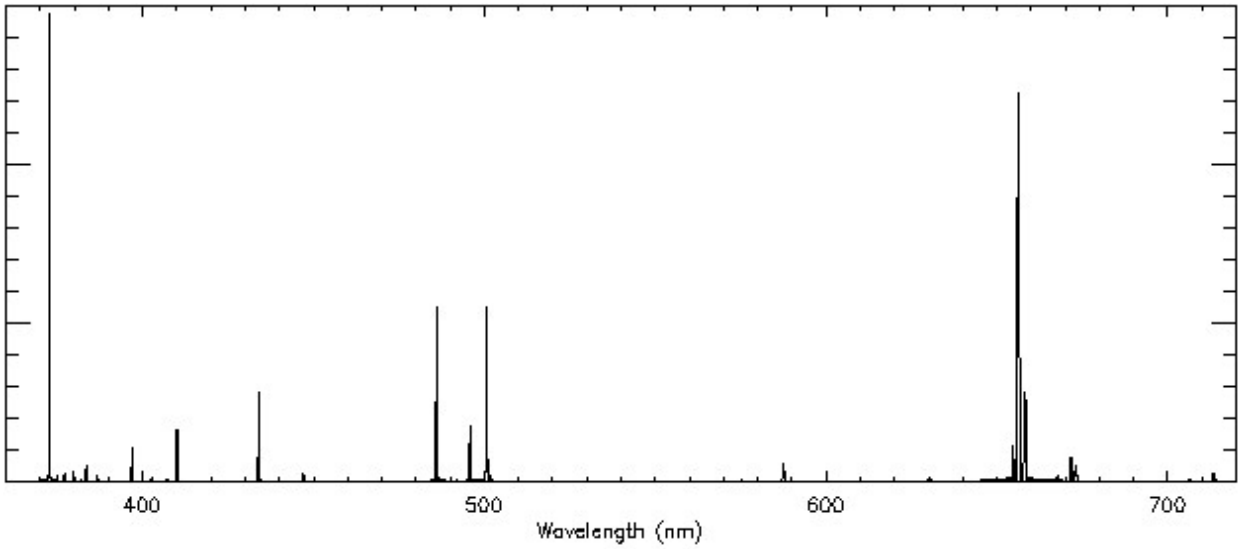

Figure 22 – Spectrum of an HII region, full spectral range. Simulated spectrum an HII region, sampled to resolve the [SII] 6716, 31 doublet (R=1440); R is twice as high in the region of [OII] 372.7 nm. This spectrum required 2550 mirror steps (single-sided interferogram with 25% before ZPD), which, taking into account the CCD readout time, only leaves ~ 2.4 s for each step (assuming a 4-h total exposure time). Only a handfull of HII regions (Orion for instance) are bright enough to be observed this way. Selecting specific ranges (650 – 680 nm to get Hα, [NII] and [SII] for example) allows a significant reduction of the number of steps.

The choice of filters selected for SITELLE therefore has to maximize the scientific output while minimizing the number of steps required to reach the spectral resolution goals. A list of filters planned for SITELLE, their transmission curves and the folding parameters used are given in Appendix C.

5.4 - Maximum and typical spectral resolutions

Although SITELLE's interferometer is theoretically capable of obtaining spectra with a maximum spectral resolution varying from R = 10 000 at 900 nm up to 25 000 at 350 nm (*Figure 23*), several practical constraints lower this resolution. The separation between the fringes is not uniform across the field of view (because of the off-axis configuration), and the contrast between fringes diminishes as the OPD increases. Moreover, image quality (set by the optics and the seeing) also lowers the maximum resolution at very high values of R. Finally, the faintness of some sources naturally limits the number of steps, and therefore spectral resolution, in order to collect enough photons at each step.

Given our experience with SpIOMM on different targets (galactic nebulae, nearby HII regions, star clusters), SITELLE's typical niche ranges from R ~ 500 (detection of faint cosmological sources, wide band in the blue-green) to R ~ 3000 (kinematics of Galactic HII regions, nearby galaxies or star clusters).

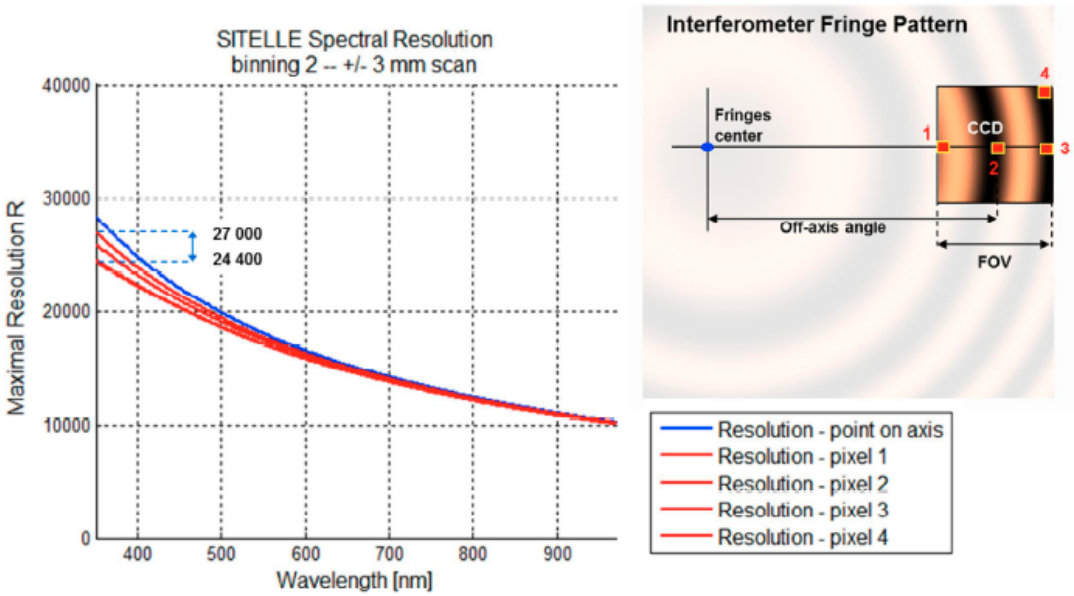

Figure 23 – Maximum theoretical spectral resolution for SITELLE. The maximum possible resolution depends on wavelength, location on the field of view and seeing/binning.

6 - Data Reduction and post-processing

Although quite simple on paper (taking the Fourier transform of the interferogram collected on a given pixel), transforming a series of interferometric images into a fully calibrated spectral data cube is not an easy task and it takes a very long time.

6.1 – ORBS

The result of each observation with SITELLE is made up of two interferometric data cubes which need to be merged, corrected, Fourier transformed and calibrated in order to get a spectral cube of the observed region ready to be analysed. ORBS[2] is a fully automatic data reduction software that has been entirely designed for this purpose by Thomas Martin as part of his Ph.D thesis (available, in French, at http://theses.ulaval.ca/archimede/meta/31471). The data size (up to 68 Gb for larger science cases) and the computational needs have been challenging and the highly parallelized object-oriented architecture of ORBS reflects the solutions adopted which made possible to process 68 Go of raw data in less than 11 hours using 8 cores and 22.6 Gb of RAM. It is based on a core framework (ORB) that has been designed to support the whole software suite for data analysis (ORCS and OACS), data simulation (ORUS) and data acquisition (IRIS). They all aim to provide a strong basis for the creation and development of specialized analysis modules that could benefit to the scientific community which work with SITELLE and SpIOMM.

Fully reduced data will be provided to the user by the CFHT.

A simplified structure of the data processing (*Figure 24*) can be presented as follows :

1 – Normal imagery reduction :
* Bias frame subtraction ;
* Dark correction ;
* Flatfield correction ;
* Cosmic ray removal.

These steps are identical to standard images data processing, with the exception of the cosmic ray removal which must take the presence of interference fringes on the images into account and also takes advantage of the third dimension (the interferogram).

2 – Combination of the two outputs :
* Cube alignment, using stars present in the field of view ;
* Combination of interferograms : since the two outputs carry the same information, except that they are « negatives » of each other (constructive interference in one frame, destructive in the other and vice-versa), the combined interferogram of a given pixel is given by $(I_1-I_2)/(I_1+I_2)$. This also takes into account the varying sky transmission, if any, during the cube acquisition.
* Phase correction.

3 – Calibration :
* Astrometry ;
* Flux ;

[2] **O**util de **R**éduction **B**inoculaire pour **S**ITELLE

* Wavelength.

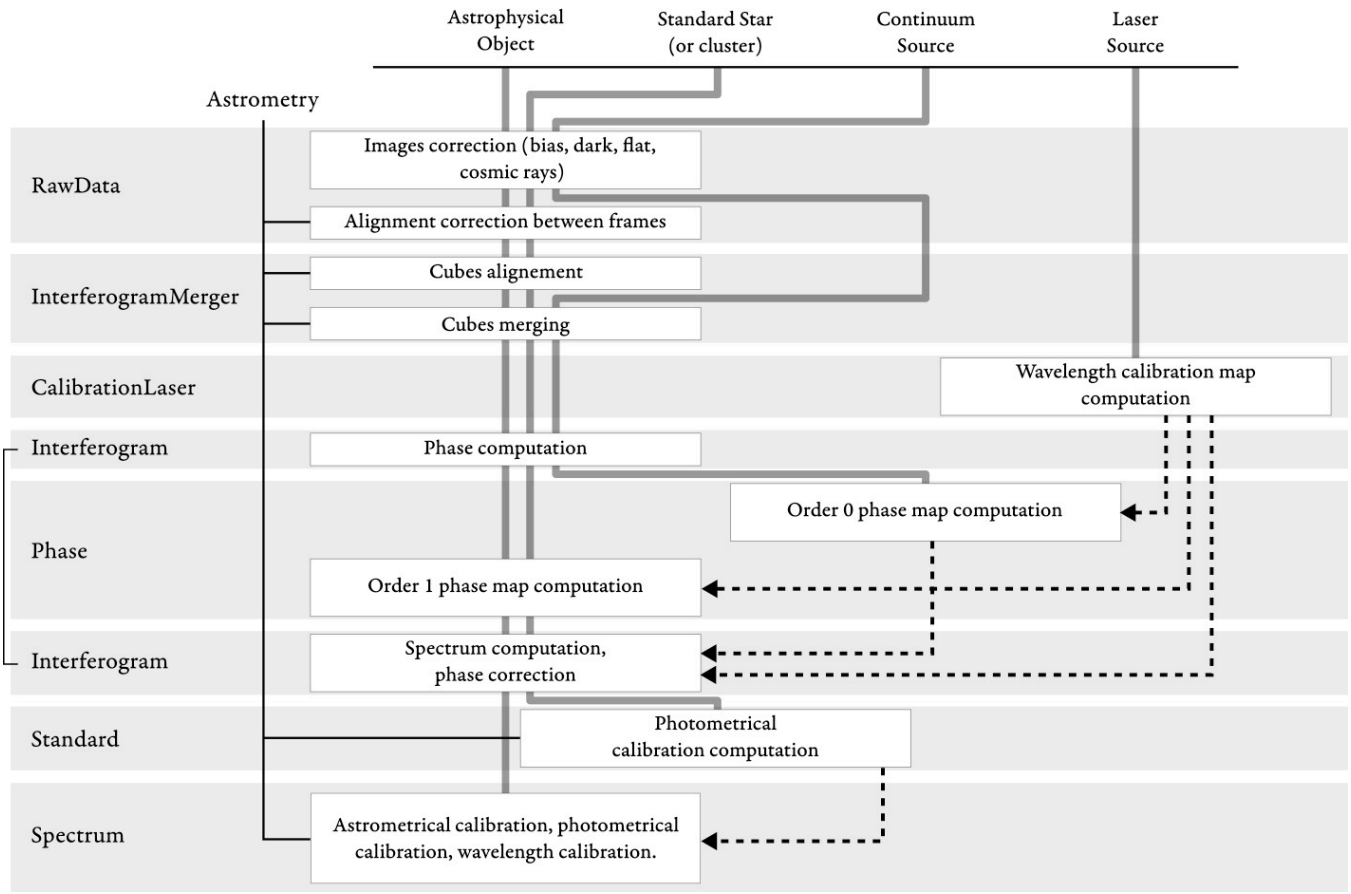

Figure 24 – Data reduction diagram for ORBS. (Fig 3.2 in Thomas Martin's thesis)

7 – Some results from the August 2015 commissioning run and January 2016 Science Verification run.

SITELLE was attached to the telescope during two runs in the summer of 2015. First, three nights in July were used for engineering (test communications with the instrument, cabling, CCD cooling) and some images through the different filters were obtained, as well as calibration laser cubes. Everything went smoothly, but a problem with the optics was obvious at first sight (see below).

Seven science datacubes were obtained during the August run (Table 7.1), aiming at testing SITELLE's capabilities, spanning a wide range of distances (10^3 to 10^9 pc), surface brightness (down to $\sim 3 \times 10^{-17}$erg/cm^2/s/pixel) and wavelength (372 nm to 680 nm). Although SITELLE's wavelength coverage extends up to ~ 900 nm, no filter redward of 680 nm were available at the time of commissioning.

A brief summary of the engineering tests is presented in section 7.1, followed by highlights from these cubes in section 7.2.

Table 7.1: Science data obtained during commissioning

Date	Target	Filter	R	# steps	Exp. time (h)
08/05	M 31 (center)	SN2	400	116	0.97
08/07	M 57	SN3	2660	593	2.47
08/07 + 08	Stephan's Quintet	SN3	1500	342	2.37
08/08 + 09	Abell 2261	C1	440	278	2.70
08/08	NGC 628	SN3	1510	323	2.24
08/09	M 1-71 (standard NP)	SN3	1520	269	0.60
08/09	NGC 6992	SN1	820	144	0.80
08/09	Abell 168	SN3	850	166	1.61

7.1 - Engineering and instrument quality

7.1.1. Servo system

Robustness - Robustness of the servo system is very good as only one loss has been experienced during commissioning. This loss was due to a bad set point of the piezoelectric actuators offset. Therefore the piezos could not use their full correction range. This type of loss is not likely to happen again because the set point will be adjusted at the beginning of each run.

Stability - Stability of the moving mirror (~20-30 nm rms, currently limited by vibrations from the cooling system of the detectors) reflects the efficiency of the servo loop on both the software and hardware sides. It is limited to 30 Hz for mechanical reasons. If the moving mirror is unstable, the modulation efficiency varies during the acquisition of the interferograms, which reduces the mean modulation efficiency (by ~ 5% @ 543 nm) and produces noise or ghosts in the resulting spectra (ghosts are replica of the real spectrum and their amplitude is proportional to it). The measure of the ghosts' amplitude is a direct measure of the servo stability. Looking at the high SNR data obtained from science and calibration cubes (Figures 7.1 and 7.2) we can see no evidence of ghosts over 0.5% of the spectrum amplitude, which is well within specs (the requirement is of 1%).

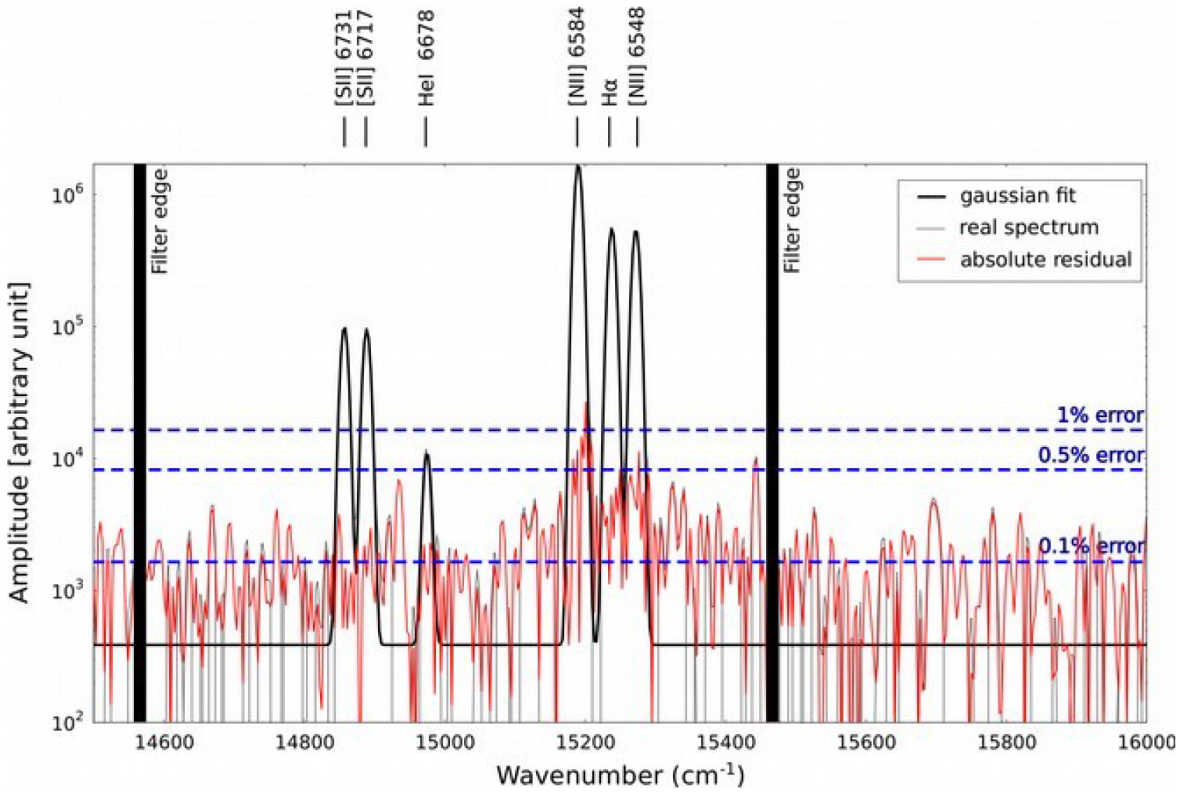

Figure 7.2: Gaussian fit on M57 spectrum (unbinned). The absolute residual shows no presence of ghosts over 0.5% of the amplitude of the brightest emission line. The general level of noise is around 0.1%.

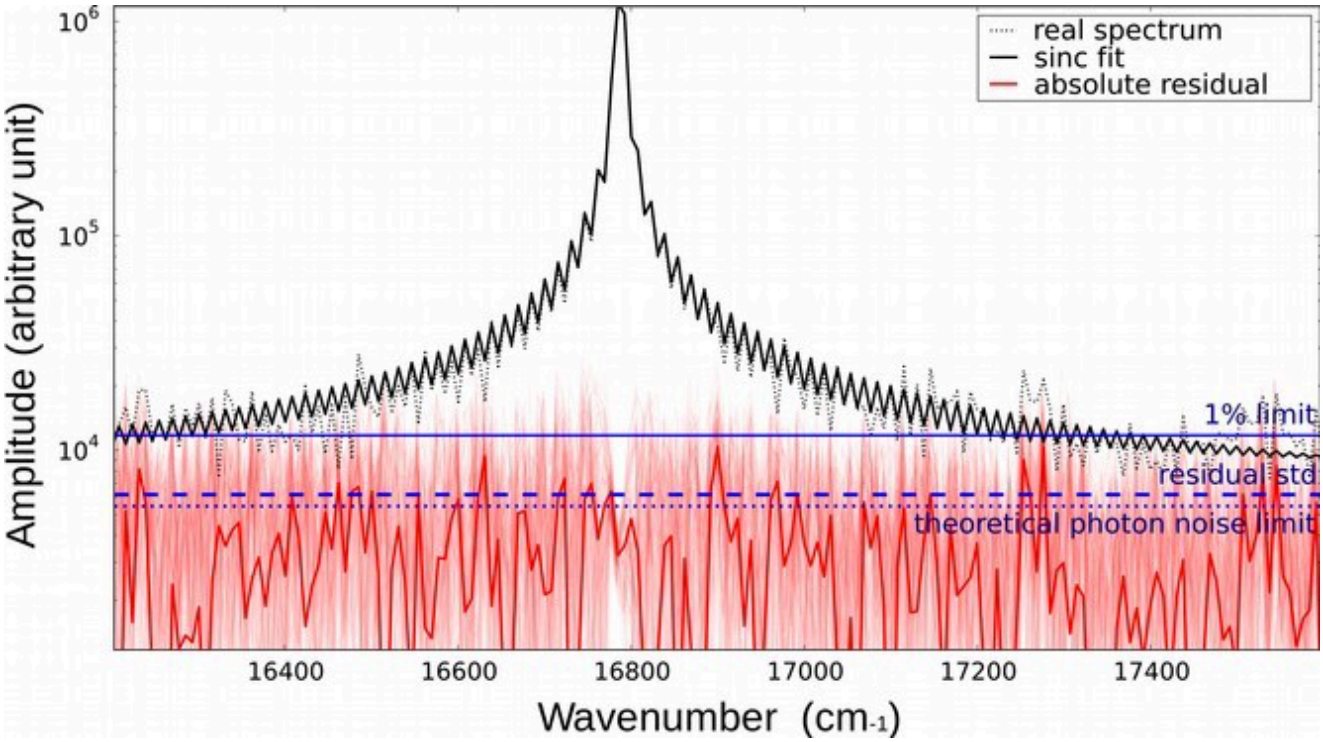

Figure 7.2: Fit of an unapodized sinc line to the green HeNe laser @543.5 nm. The residual has been computed from 100 different pixels of the same laser cube obtained at the end of the run. There is no evidence for ghosts over the 1% limit. Note also that the mean residual standard deviation lies slighlty above the theoretical photon noise limit (+ 20 %) which demonstrates that, for high SNR data, noise coming from servo instability (which scales linearly with the brightness of the source) is still negligible.

7.1.2 Instrument photometric throughput

The total instrumental throughput (instrument + telescope + atmosphere) has been measured by photometry of 2 standard stars observed through all SITELLE's filters (Table 7.2). The expected number of counts in each filter has been simulated with the ETC using a calibrated standard star spectrum. Given the uncertainty on the optical transmission and telescope mirrors reflectance variations (simulated by a simple flat curve at 50%), it is worth noting that, except for the blue filters (SN1, C1) the error is always less than 10%. The average 15% loss in the blue part of the spectrum has also been measured in Megacam images and is mostly due to the aging of the telescope mirror coatings. SITELLE's overall throughput is shown in Figure 1.

Table 7.2: Spectrophotometric standard stars observed during commissioning

	GD248			***G24-9***		
Filter	**Observed counts (s^{-1})**	**Simulated counts (s^{-1})**	**Error (%)**	**Observed counts ($10^4 s^{-1}$)**	**Simulated counts ($10^4 s^{-1}$)**	**Error (%)**
SN1	*4400*	*5600*	*-21%*	*1670*	*1840*	*-10%*
SN2	*10000*	*10700*	*-7%*	---	---	---
SN3	*8000*	*8650*	*-7%*	*4800*	*5200*	*-8%*
C1	*31450*	*34310*	*-8%*	*11142*	*13850*	*-23%*
C2	*16000*	*16000*	*--*	*9200*	*9200*	*---*

7.1.3 Modulation efficiency

Modulation efficiency (ME) reflects the quality of the interferometer. With a perfect interferometer, all the input light must be modulated (ME=1). In this case the contrast between two consecutive fringes of an interferometric image taken far from ZPD must be maximum (the minimum of the fringe must be 0 and the maximum must equals the brightness of the source). Very far from ZPD (R > 15 000) modulation efficiency is likely to decrease because the size of the fringes becomes comparable to the size of the seeing disk. But if everything goes well it must be relatively flat for resolution < 10 000.

Looking at laser interferograms, which must have the shape of a sine, the contrast between two consecutive periods gives the modulation efficiency at a certain OPD. For reasons still unknown we can see that modulation efficiency decreases too fast and becomes bad at a moderate distance from ZPD in one particular direction (Figure 7.3).

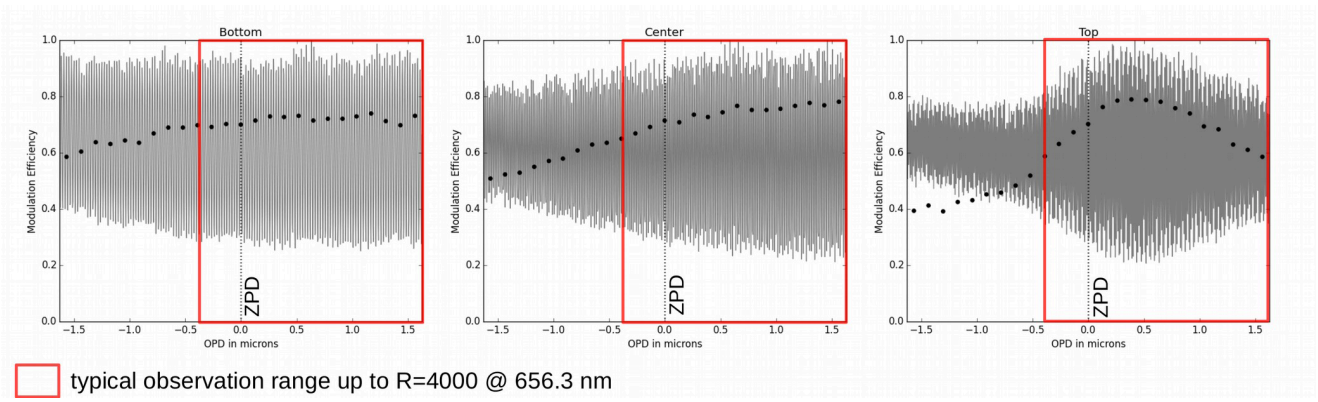

Figure 7.3: Evolution of the modulation efficiency with the OPD. As the OPD increases, ME decreases but one side is far better than the other. The interferogram from which the ME curve has been calculated is shown in grey.

Measuring the contrast between fringes on an image taken far from ZPD gives a map of the modulation efficiency at the OPD of the image. Figure 7.4 shows such a map measured at a distance from ZPD which corresponds to a resolution R ~ 4000 @ 656.3 nm (the image corresponds to the very end of the laser cube used in figure 7.3). We can clearly see a loss of ME from bottom to top and that reflects perfectly what we can see in figure 7.3.

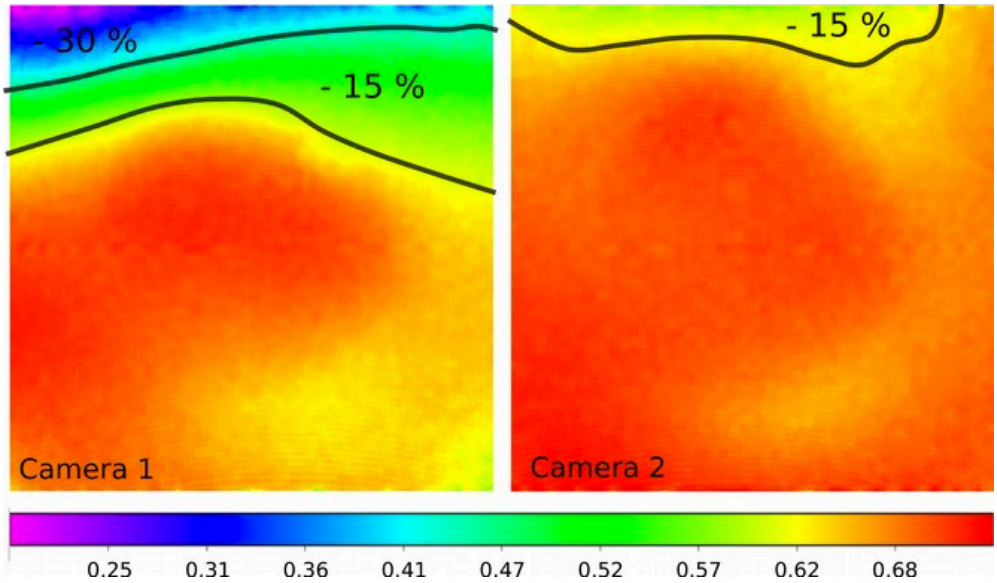

Figure 7.4: Map of the modulation efficiency far from ZPD (R ~ 4000 @ 656.3 nm) over the entire FOV in camera 1 and camera 2 before the camera adjustment in October 2015. Regions with -15 % and –30 % ME loss are represented. These maps have been derived from a laser cube (laser wavelength: 543.5 nm).

Impact of reduced ME on science

The impacts of the varying ME as a function of OPD can be summarized as follows:

Because the Line spread function (observed as the FWHM of unresolved emission lines) "builds up" as the mirror moves to higher OPDs, a decrease in ME by 50% at large OPD translates into a relatively minor (~ 10%) increase in the lines' FWHM and SNR over most of the field of view (see

Figre 7.5). The worst case scenario therefore involves observing a target that completely fills the FOV and that is bright enough to allow observations at high spectral resolution (bright galactic nebulae such as Orion or M16). Cubes with a required spectral resolution R < 2000 are not affected by this issue.

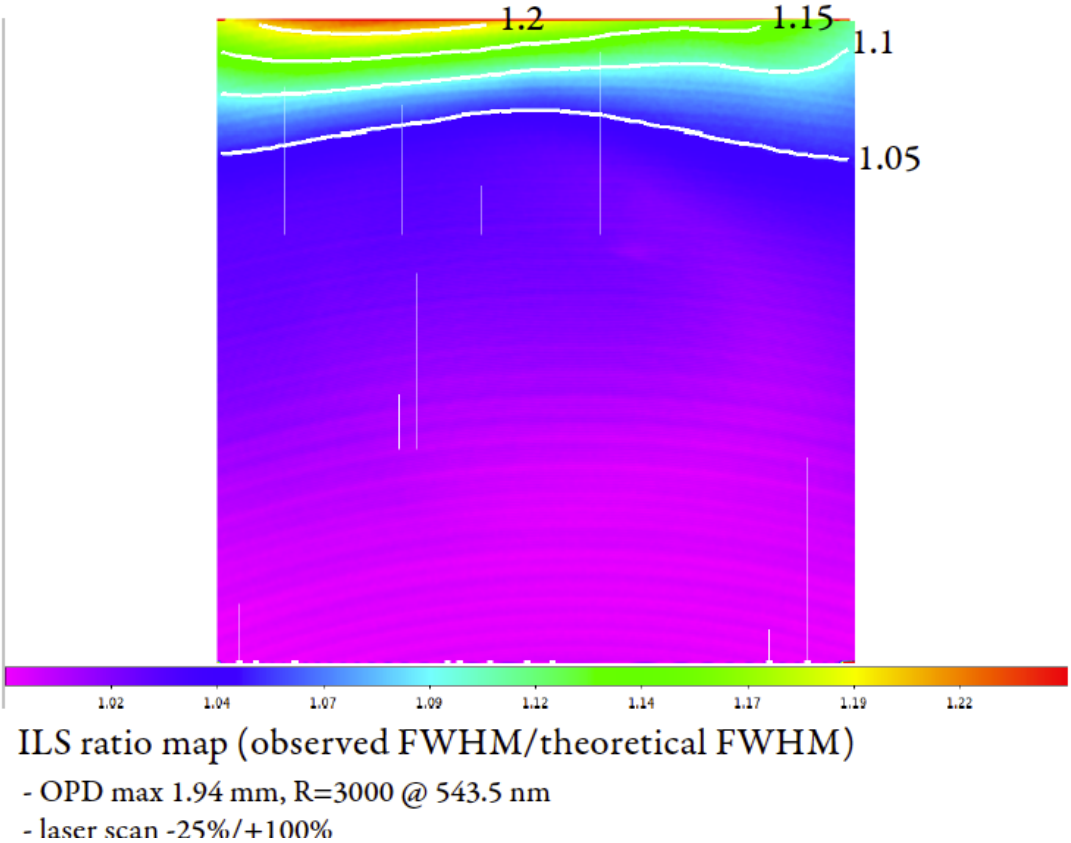

Figure 7.5: Instrument line spread function ratio map at R=3000, illustrating the loss of spectral resolution as a function of the location in the field of view.

7.1.4 - Image quality

Image quality was by far the biggest issue after commissioning because it is far below specifications in the upper part of the image and in the lower right corner (figures 7.6 and 7.7). Two problems were detected early on:

1 - A strong degradation (inverse coma) of IQ in the uppermost section (300 pixels) of both cameras. IQ in the lower section (300 pixels) of both cameras is not ideal, but the degradation is not as bad as in the upper part. There is therefore a strong asymetry in the optical defect. Although the core of the PSF is sharp and contains most of the light, up to 15-20% of the PSF flux is spread over the extended tail.

2 - In the affected zones, IQ is worst in CAM1 than in CAM2 (Figure 7.6)

Both cameras were returned to U. Laval in October, where a tilt (25 µm) in one of the lenses in CAM1 was discovered using a double-pass Zygo test. The lens was recentered.

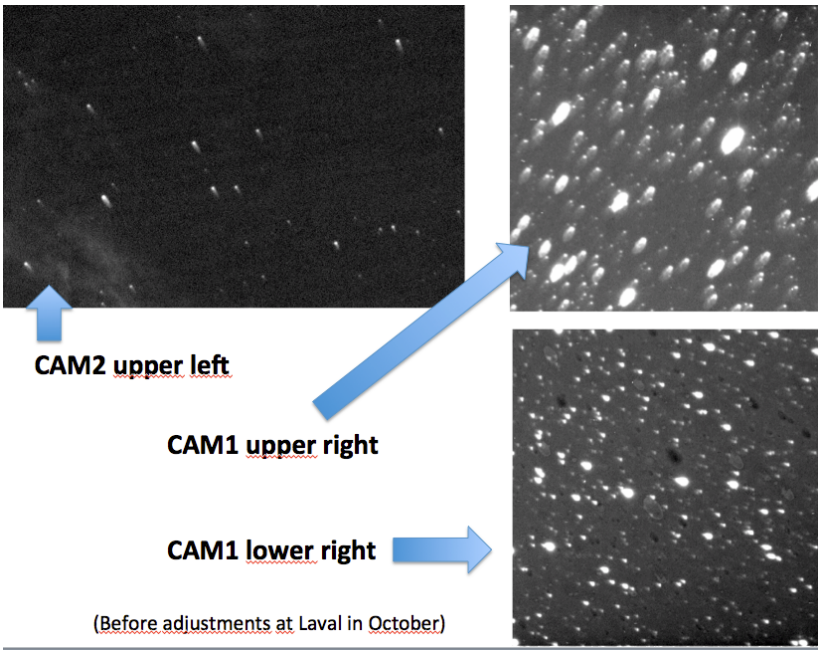

Figure 7.6: Ilustration of the image quality problem detected in the corners of the images in the two cameras.

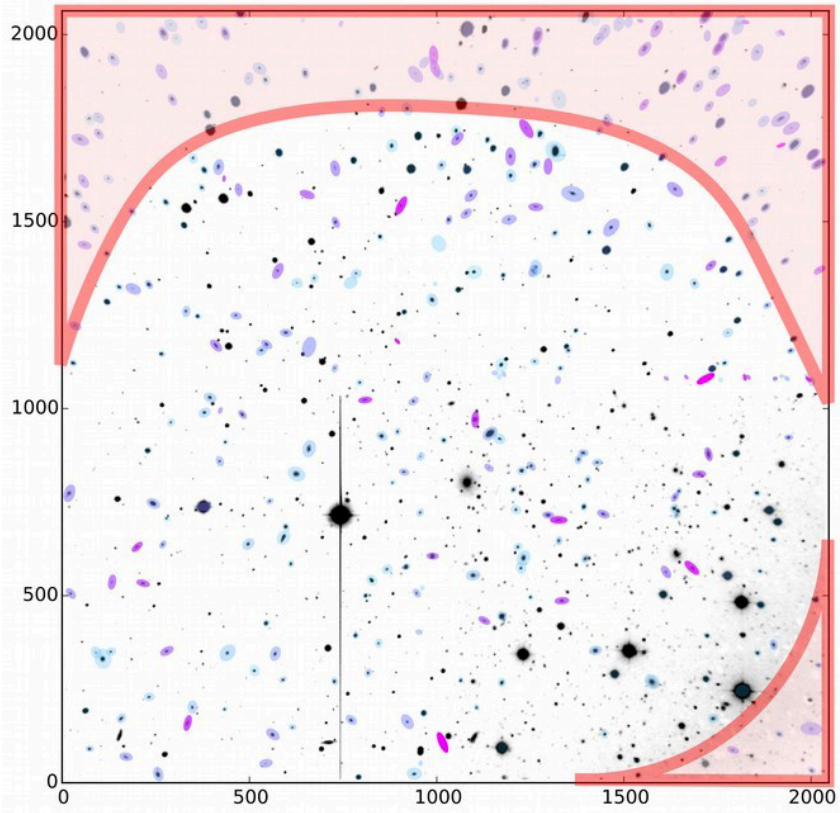

Figure 7.7: Strongly distorted regions of the field (in red) have been superimposed onto an image of Abell 2261. Ellipses measured with Sextractor onto the brightest stars are also shown (andmagnified). The affected regions show stars elongated and pointing toward the center of the field.

The IQ and ME problems are under investigation at the time of writing. To summarize their impact on the science:
- Targets spanning a FOV less than 9' x 9' and requiring R < 2500 are not significantly affected.

7.2 - Science

Following is a representative sampe of the science data obtained duting commissioning and Science Verification phases.

7.2.1 - M57/IC1296, SN3 filter:

Objectives:

- Demonstrate R > 2500 and SITELLE's capability to maintain a good modulation efficiency for ~ 3 hours and > 600 mirror steps;
- Observe two targets at very different redshifts in the same cube (M57 and IC 1296);
- Detect eventual ghost lines and fringes caused by the very bright emission lines in the ring;
- Detect the faint HeI 6678 emission line near the ~ 200 times brighter Hα and [NII] lines.

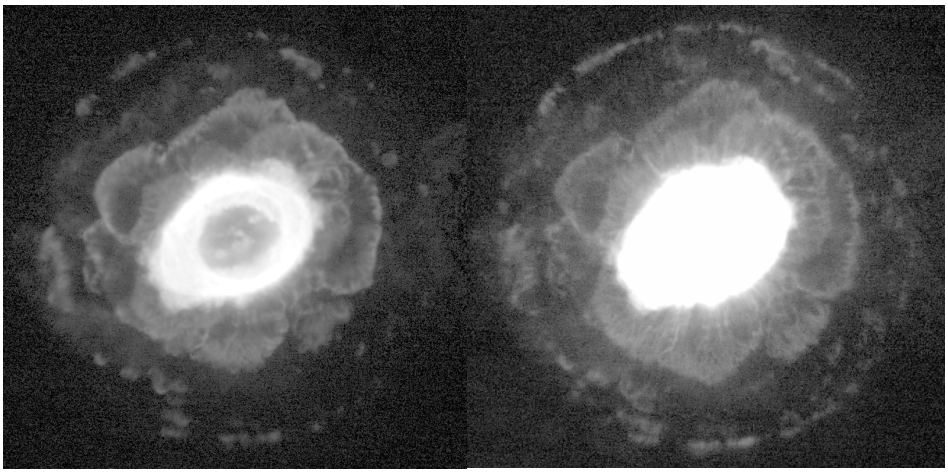

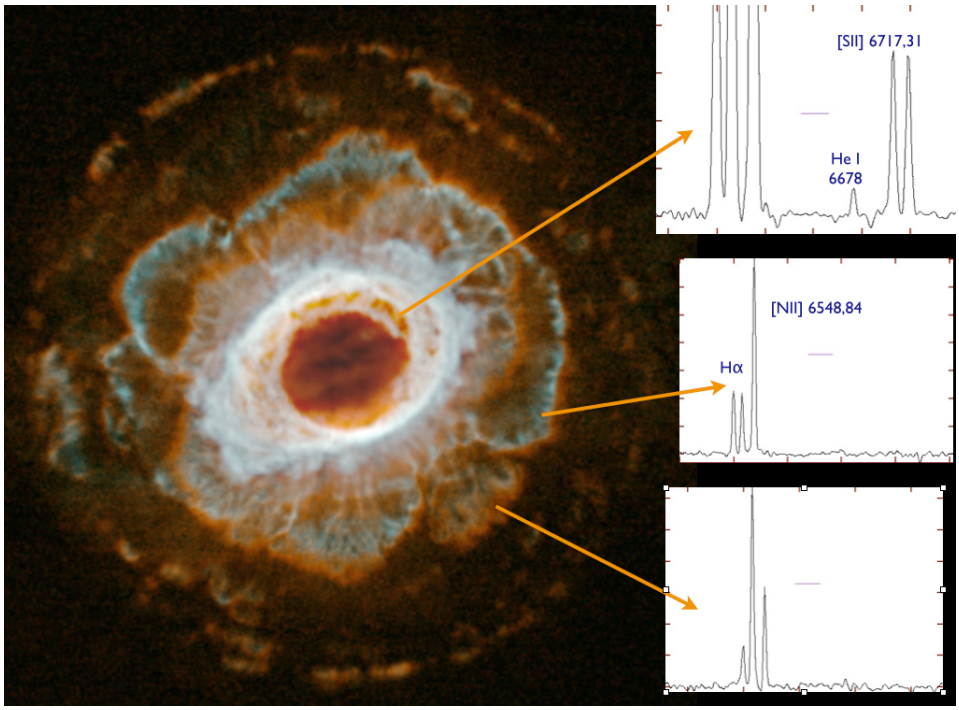

Figure 7.8 : Monochromatic images of the planetary nebula M57 at [NII] 6584 (upper left) and Hα (upper right), a color-coded combination (red: Hα, blue: [NII]) and examples of spectra.

Discussion:

Although M57 is a very well-known Messier object, SITELLE has obtained the most detailed spatially-resolved spectra of this planetary nebula ever obtained. The same cube has allowed to determine the rotation curve of IC 1296 (z=0.017) as well as to obtain, for the first time, a map of its oxygen abundance. In both cases, a complementary cube with the SN2 filter is desirable to complement the analysis.

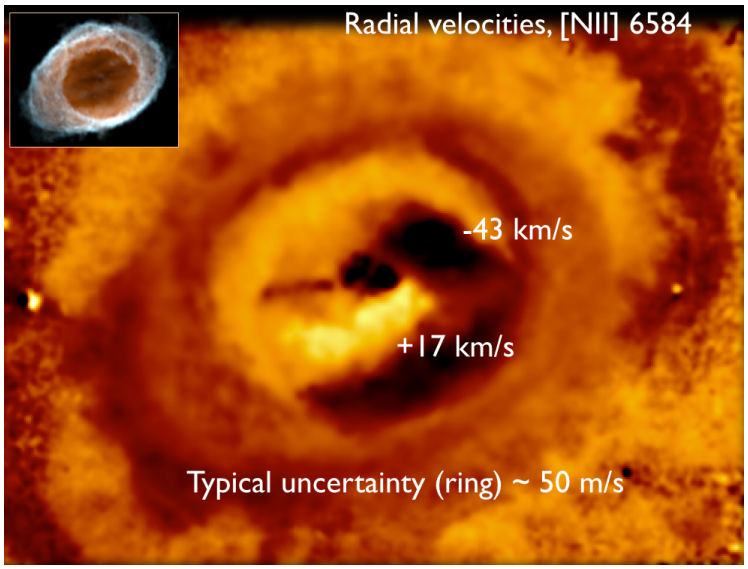

Figure 7.9: Doppler image of the central part of M57 (insert: color-coded image of the same field) showing the radial velocities as measured in the [NII] 6584 line.

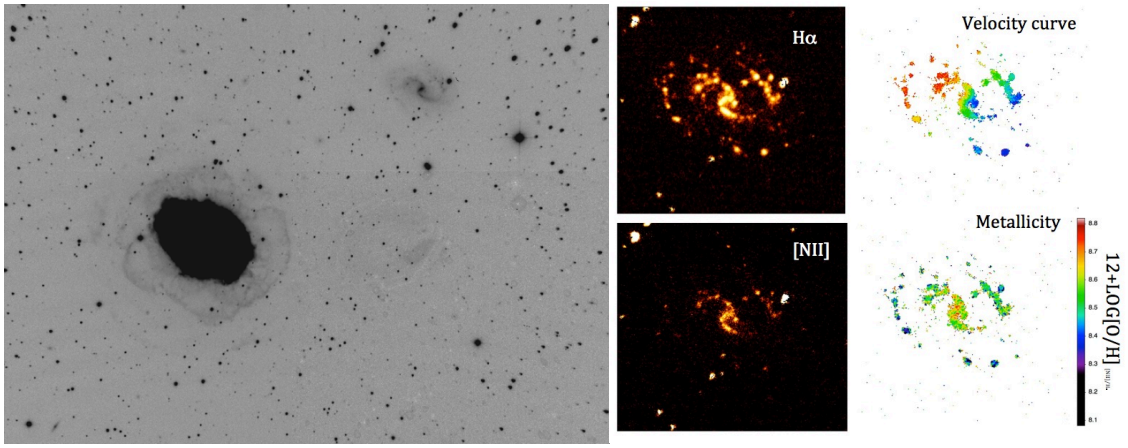

Figure 7.10 : (Left) Part of the SITELLE FOV showing M57 and the nearby spiral galaxy IC 1296. (Right): Monochromatic intensity maps of IC 1296, and the velocity curve and metallicity maps derived from the same cube as the M57 data shown above.

7.2.2 - NGC 6992, SN1 filter:

Objectives:

- Demonstrate SITELLE's capability to obtain spectra in the 350 - 380 nm region;
- Map the oxygen abundance variations across the nebula.

Discussion:

SITELLE was designed to optimize its performance in the near-UV with a specific goal: to detect the very useful [OII] 3727 diagnostic line. With an excellent modulation efficiency of 60% at 370 nm and a good CCD quantum efficiency (65%) at the same wavelength (90% at 600 nm), SITELLE has a very clear advantage compared to other IFUs such as MUSE in this wavelength range, not to mention its much wider, contiguous field of view.

The oxygen abundance map shown of a section of the Cygnus Loop's old supernova remnant below has been derived by combining SITELLE's SN1 cube with SpIOMM's cubes at other wavelengths and using shock models provided by the MAPPINGS code.

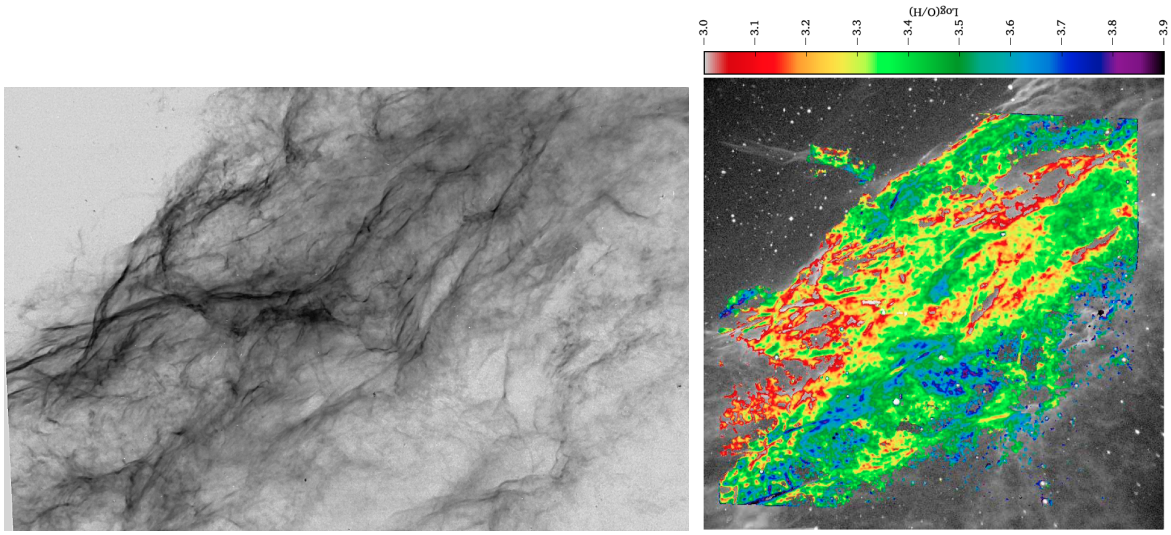

Figure 7.11: SITELLE [OII] 3727 image of a section of NGC 6992 (left), and the derived oxygen abundances (right) determined by combining the SITELLE cube with SpIOMM data.

7.2.3 - M31, SN3 filter:

Objectives:

- Demonstrate SITELLE's capability to recover emission-line sources superimposed on a bright continuum;
- Demonstrate SITELLE's capability to determine the radial velocities of known planetary nebulae;
- Detect the very faint, diffuse [OIII] gas "spiral" previously detected in Hα;
- Demonstrate SITELLE's ability to detect the Hβ absorption line from the unresolved stellar population

Discussion:

Although FTS are very efficient at detecting emission lines, they suffer from distributed noise (Maillard et al. 2013, Exp. Astr. 35, 527), making them vulnerable to the presence of a strong continuum. The extended core of the Andromeda galaxy thus provided a good target to test SITELLE's ability to recover known planetary nebulae (identified by their strong [OIII] 4959,5007 emission) superimposed on a strong background. M31's cube was the first ever obtained with SITELLE, at the end of one night. Because of the late start, it was not as deep as expected and did not reach the optimal spectral resolution planned.

Nevertheless, as Figure 7.12 shows, about 150 planetary nebulae were detected in the field of view (~ 75% completeness, based on the current catalogue of known PNs in M31); a complete cube would have reached a higher completeness level. We are currently measuring the PNs radial velocities and a comparison with a dispersive spectroscopic survey will be made. We have also detected the very faint diffuse gaseous spiral surrounding the core of the galaxy in the [OIII] line, previously detected in Hα.

Figure 7.13 shows a comparison between the [OIII] equivalent width map obtained with SITELLE in the very core of M31, where the continuum at its strongest, with a map obtained with a standard, dispersive IFU, SAURON. All known PNs in this field were recovered by SITELLE, as well as known structures in the diffuse gas.

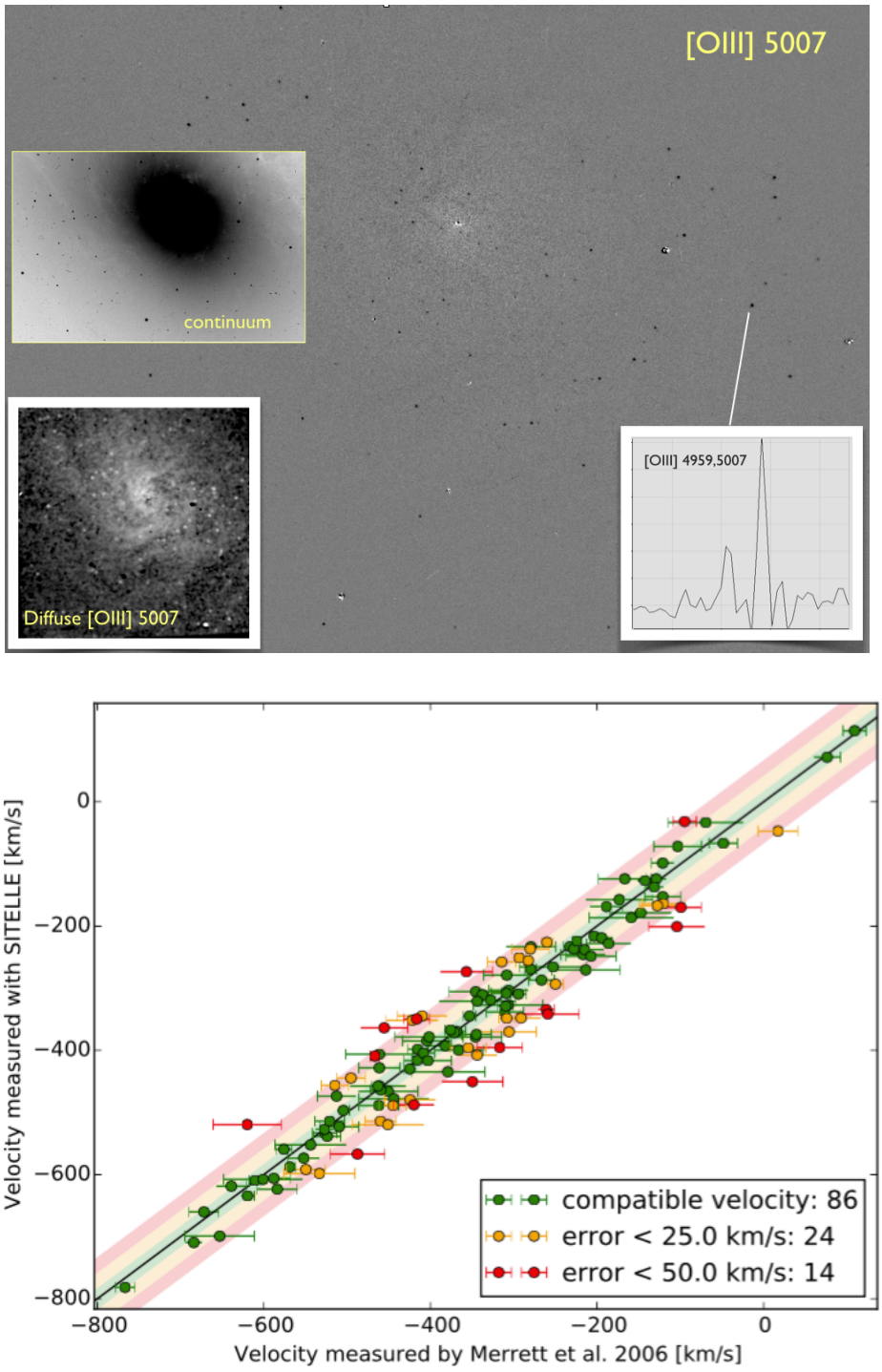

Figure 2.12: (upper panel) SITELLE continuum-subtracted [OIII] 5007 image of a section of M31. Planetary nebulae stand out as unresolved black dots. Inserts show the blue continuum image of this field from the same cube, the spiral structure from the diffuse [OIII] emission, as well as a spectrum of one planetary nebula. (lower panel) A comparison between the radial velocity of the planetary nebulae measured with SITELLE and that of Merrett et al (2006).

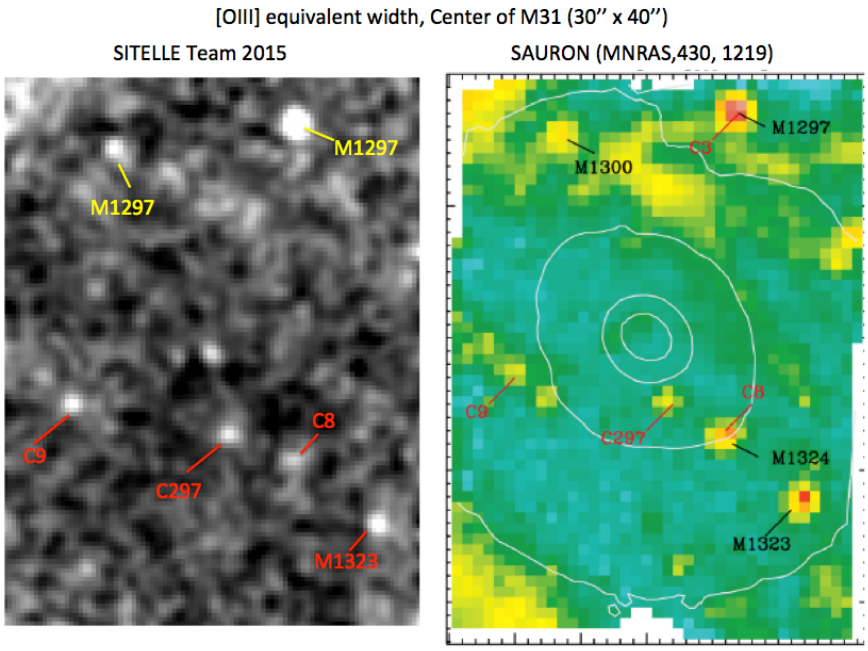

Figure 7.13: Comparison of the SITELLE [OIII] 5007 equivalent width from a small section around the nucleus of M31 with the the same map from the SAURON IFU attached to the 4.2-m WHT. Planetary nebulae are identified, and the diffuse gas is also detected.

7.2.4 - NGC 628, SN3 filter:

Objectives:

- Compare SITELLE's data with those of other IFUs on a well-studied extended spiral galaxy;
- Measure the Hα surface brightness detection limit;
- Measure the global metallicity gradient, as well as local variations in the nebular parameters on small scales.

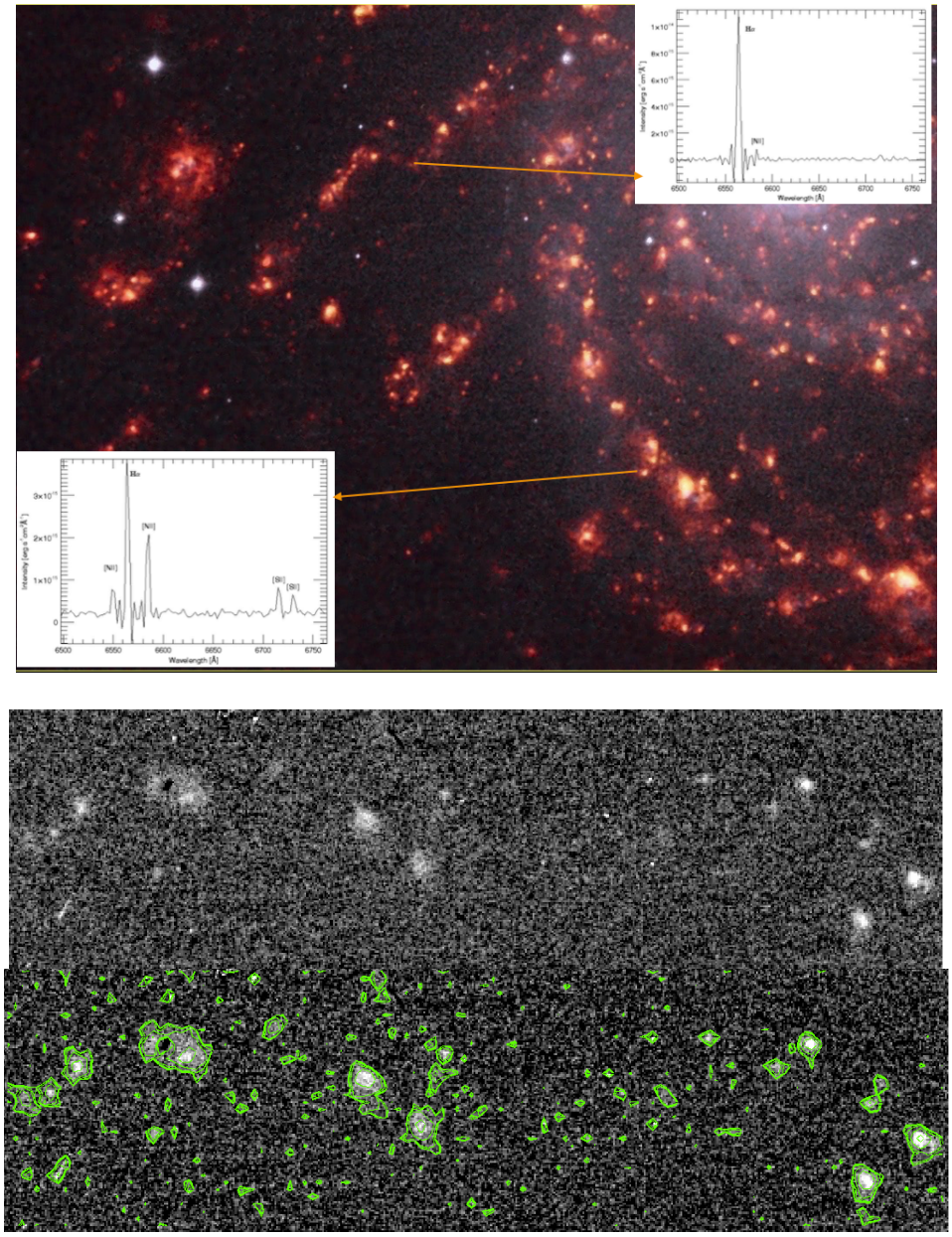

Figure 7.14 - (Upper panel) Image of a section of NGC 628's external spiral arm extracted from a SITELLE cube with inserts showing spectra of HII regions with two different metallicities. (Lower panel) Continuum-subtracted Hα image without and with contours of the faint, northern arm.

Discussion:

NGC 628's gaseous content has been studied in detail, with narrow-band filters and dispersive IFUs, and thus provided an excellent target for a detailed comparison for SITELLE. This data cube has clearly shown that SITELLE was able to detect very faint HII regions in the oustkirts of the galaxy (Fig 2.14, lower panel), and that its spatial resolution and large contiguous field of view provide a net advantage over other IFUs. Cubes were also obtained during the SV run in January 2016, in the SN1 ([OII] 3727) and SN2 (Hb, [OIII]) filters - data are being reduced and analysed.

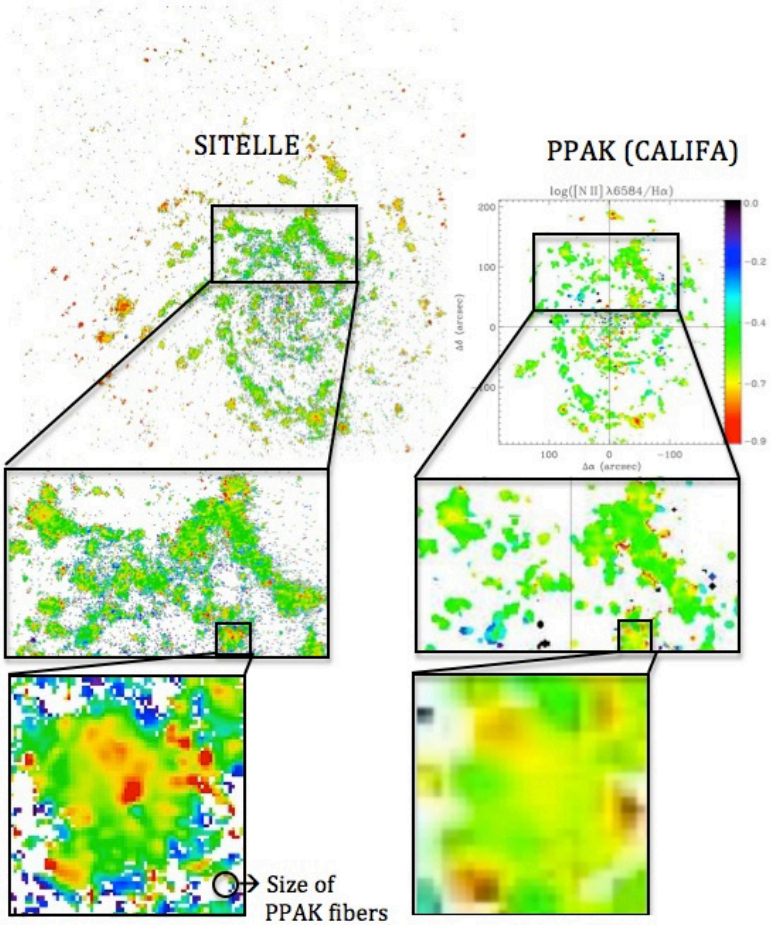

Figure 7.15 - Comparison of the [NII]/Hα ratio in NGC 628 between SITELLE (one single field) and PPAK (CALIFA project - 20 fields) demonstrating SITELLE's clear advantage in terms of spatial resolution and contiguous field of view.

2.5 - Stephan's Quintet, SN3 filter:

Objectives:

- Two targets at very different redshifts (NGC 7320 and the other galaxies);
- Detect and characterize faint tidal tail Star-forming regions;
- Allow a direct comparison with data obtained with a standard IFU (PPAK);
- Demonstrate SITELLE's capability to obtain two sections of the cube on consecutive nights and combine them.

Discussion:

Stephan's Quintet is another well-studied object, rich in ionized gas of different origins (photoionization, shocks, AGN), with a very complex kinematical structure and is therefore a target of choice for SITELLE's commissioning. Analysis of the cube is underway, but we can confirm SITELLE's ability in detecting pockets of ionized gas up to large distances from the main bodies of the galaxies and measure their radial velocity with an excellent precision. Absorption features are also detected in the core of NGC 7318A (Figure 7.16).

A very important observing mode has been tested on this target: start a cube on one night and continue it the night after. Because of very stringent requests on mirror positioning and the position of the Zero Path Difference, this was not possible with SpIOMM, SITELLE's prototype. We thus obtained one part of the cube on one night, the second part the next night. The final cube does not show any evidence for mirror positioning errors, which would have been detected as abnormal structures in the emission lines.

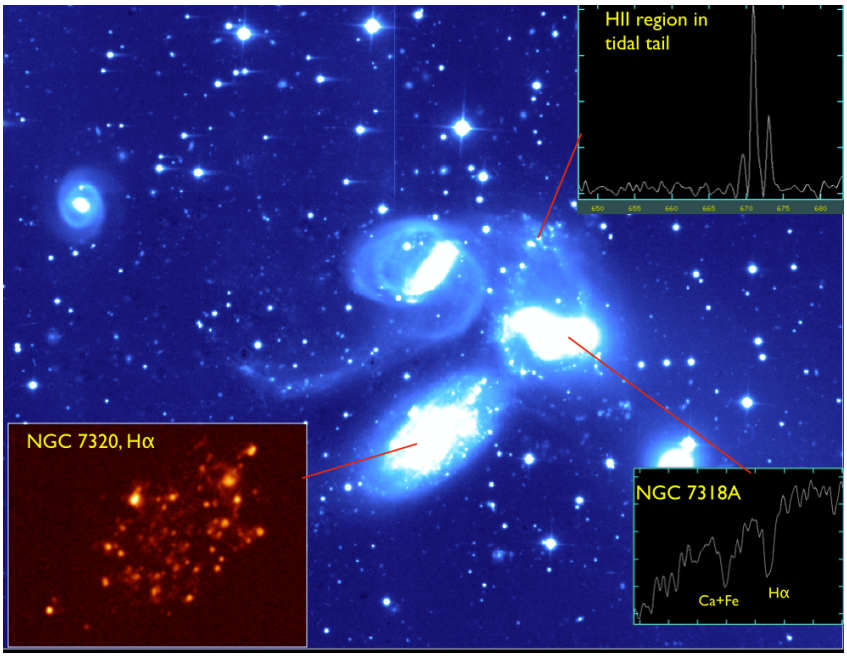

Figure 7.16 - Deep image of Stephan's Quintet from a SITELLE cube, with inserts showing spectra of an HII region in a tidal tail, absorption lines in the core of NGC 7318A, and the continuum-subtracted Hα image of the foreground galaxy NGC 7320.

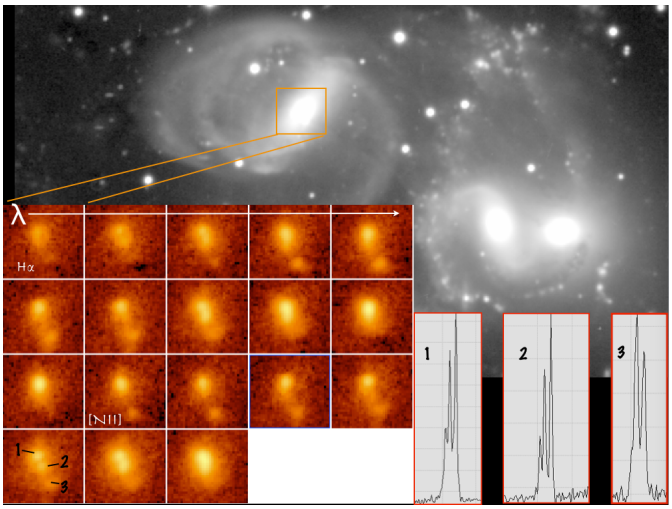

Figure 7.17 - Monochromatic images of the AGN and jet at the core of NGC 7319 redward of the Hα and [NII] lines showing their kinematics; spectra of three knots in this region are also shown.

7.2.6 - Abell 2261, C1 filter:

Objectives:

- Characterize the C1 filter
- Detect the redshifted [OII] 3727 emission line in star-forming galaxies

Discussion:

C1 is the widest filter tested during commissioning. With an FTS, the wider the filter is, the lower the spectral resolution can be for a given number of mirror steps. C1 has been designed, among other things, to detect the star-formation diagnostic [OII] emission line at redshifts 0.05 - 0.33. Abell 2261 is a massive galaxy cluster. The [OII] line has been detected in ~ 30 galaxies; in most cases, the emission is extended, as shown by the inserts in Figure 7.18. Absorption lines (in particular Ca H& K) have also been detected in foreground galaxies.

We note that a very quick inspection of several cubes obtained with the C1, SN2 and SN3 filters aiming at a nearby target reveal the presence of several previously uncatalogued distant star-forming galaxies through the presence of their redshifted [OII] emission line.

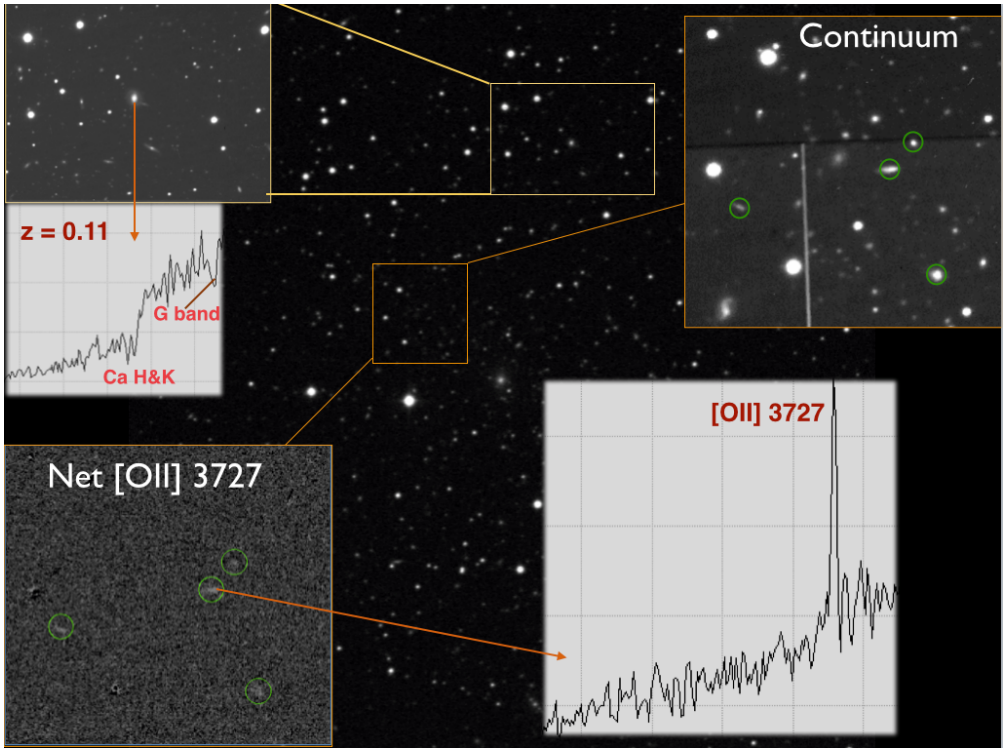

Figure 7.18 - Sections of SITELLE's cube of Abell 2261 (background: DSS; inserts: SITELLE), showing, in the upper left corner an image and spectrum of a foreground galaxy at z=0.11 (redshift determined from the Ca H&K, Hδ, and G-band absorption features). Upper right and lower left inserts: continuum and net [OII] emission, respectively, showing extended [OII] emission in four galaxies (circled in green), accompanied by the spectrum of one of them, clearly showing the [OII] line.

7.2.7 - M42, SN1 filter (Science verification, January 2016 - Data still being reduced)

Objectives:

- Characterize the SN1 filter
- Demonstrate SITELLE's capability to separate the [OII] 3727 doublet in galactic HII regions to determine the electron density.

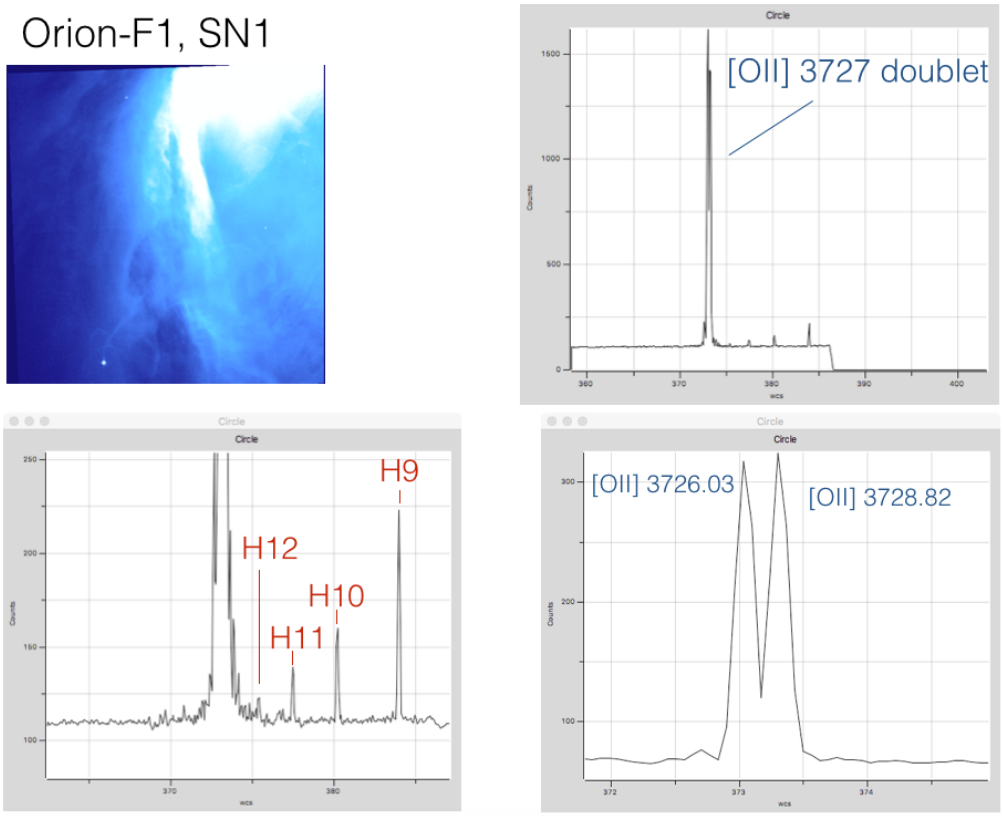

Figure 7.19 - [OII] 3727 image of a small section of the Orion nebula with details of the spectra for a few regions.

Appendix A - Detectors

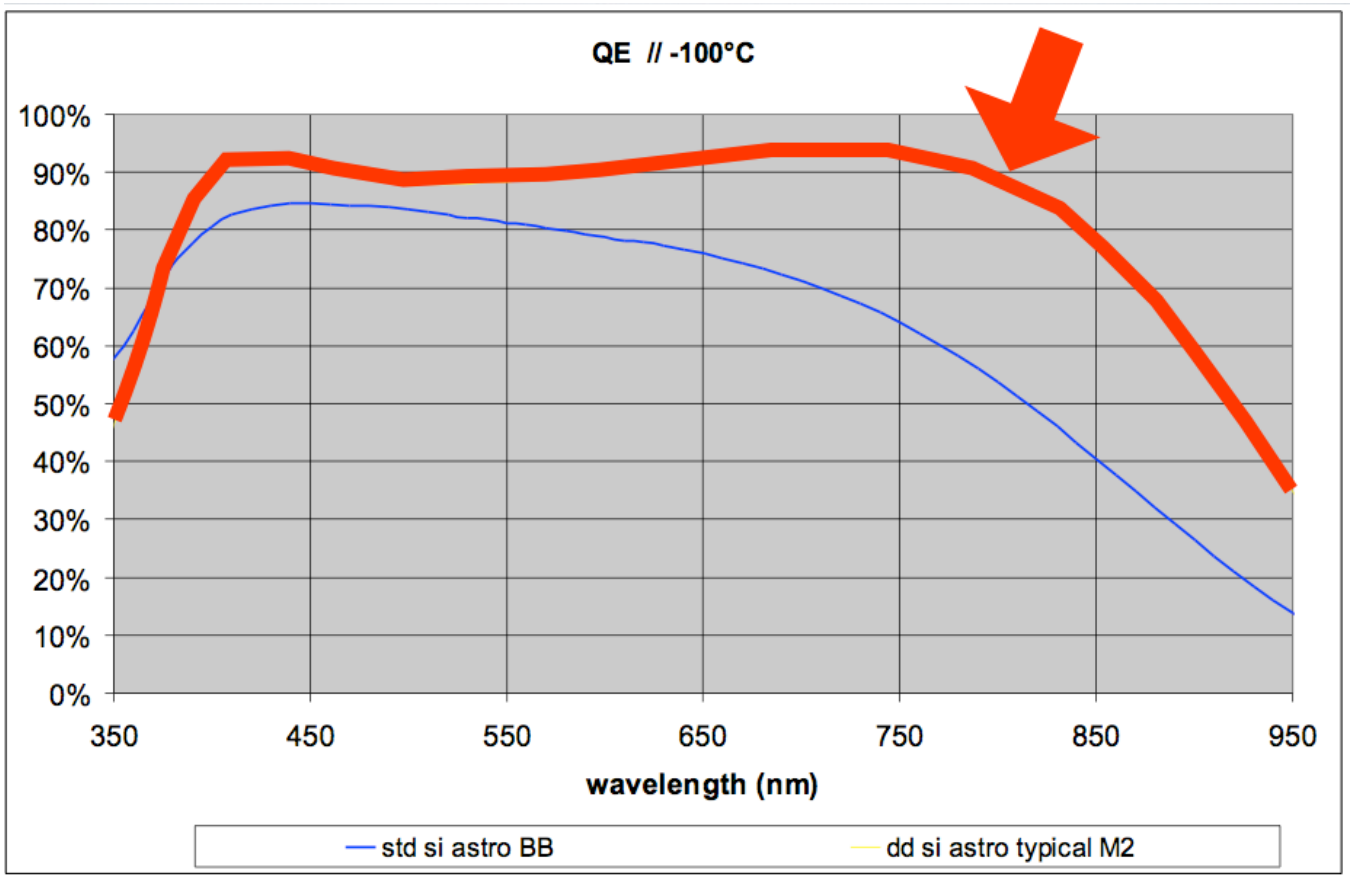

Figure A1 – SITELLE's CCD quantum efficiency. (Red curve)

Appendix C – Filter transmission curves and parameters

Table C1 provides a list of potentially interesting filters for SITELLE, as identified during the 2013 SITELLE science workshop (http://www.craq-astro.ca/sitelle/documents.php), while their wavelength range is illustrated in Figure C1. As of January 2016, five filters (identified in red in the Table and Figure) have been ordered and received at CFHT. Transmission curves and folding order properties are presented in the following pages.

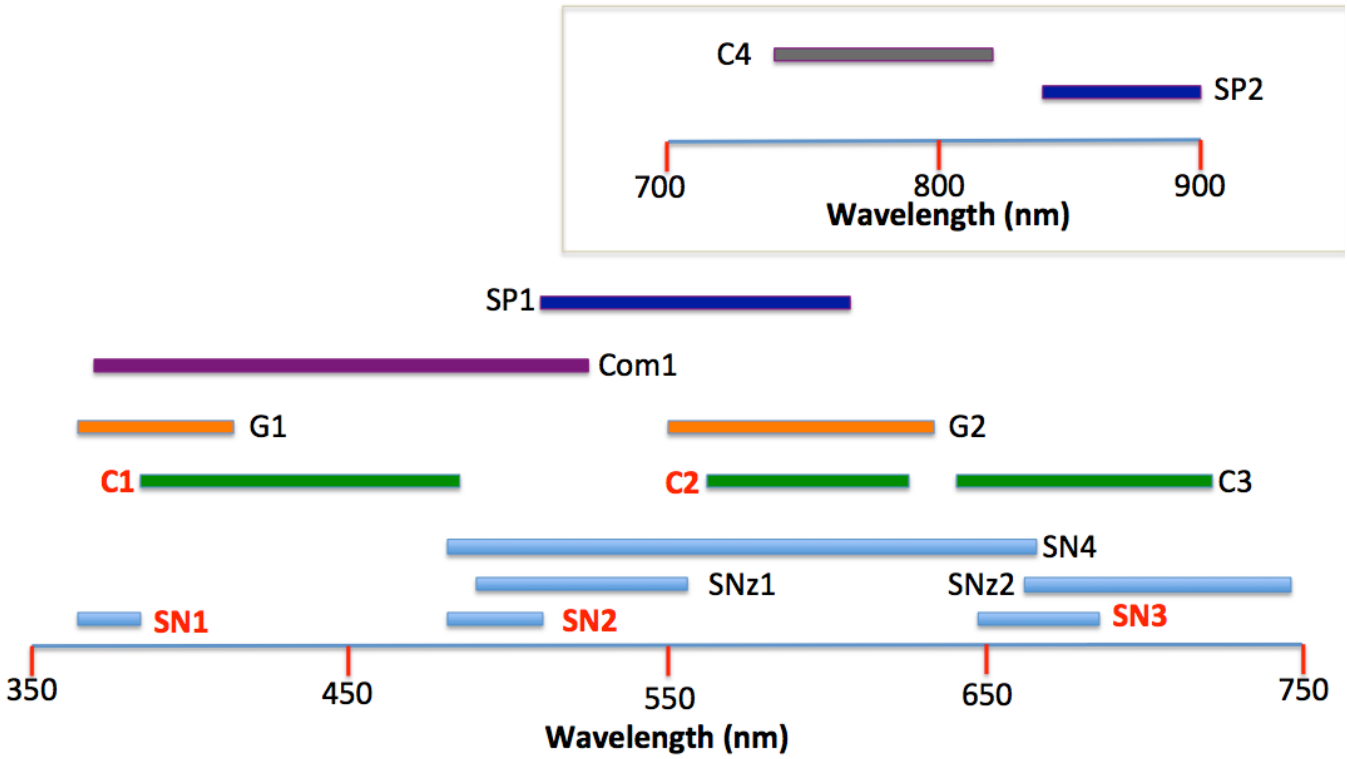

Figure C.1 – Available (red label) and potential filters for SITELLE

Table 1. Potential filter list for SITELLE

Filter Name	Waveband (nm) T>90%	Spectral lines and comments
SN1*	363-386	[OII] 3727 up to 10000 km/s; Lyα: z=1.98 – 2.17
SN2*	482-513	Hβ 4861, [OIII] 5007 up to 7500 km/s ; Lyα: z=2.92 – 3.23 Also detection & kinematics of PNs; [OII] 3727 at z=0.28 to 0.38
SN3*	648-685	[NII] 6548 to [SII] 6732 up to 5300 km/s [NII] 6584 up to 12000 km/s (z≈0.04); Lyα: z=4.33 – 4.63
SN4	481-670	Hβ 4861 to Hα 6563
SNZ1	490-556	From z=0.02 to 0.1
SNZ2	661-745	From z=0.016 to 0.1
SP1	510-607	Mg_2 5175, Fe 5270, 5335, 5406, 5709, 5782, and NaD 5890 up to 8000 km/s
SP2	840-900	CaT+PαT+TiO (as in Cenarro et al. 2009, MNRAS, 395, 1895)
G1	365-414	[OII] 3727, [NeIII]/H/HeI…, [SII] 4069,4076, and Hδ 4100
G2	550-633	Cl III 5518,5538, [OI] 5577, [NII] 5755, HeI 5876, [OI] 6300, and [SIII] 6312
C1*	389-484	[OII] 3727 from z=0.045 to 0.29; Lyα: z=2.20 – 2.98 Also Hγ 4340, [OIII] 4363, HeI 4471, Hβ 4861, CaH&K 3933/3968 (z=0 – 0.24), Gband 4300 (z=0 – 0.15)
C2*	560-626	Between sky lines ([OI] 5577 and 6300) for cosmology; Lyα at z=3.61 to 4.15; [OII] 3727 at z=0.50 to 0.68; [NII] 5755 (temprature in HII regions)
C3	640-720	Between OI auroral and strong OH lines for cosmo.: Lyα at z=4.26 to 4.92; [OII] 3727 at z=0.72 to 0.93
Com1	370-525	CN, C3, C2, and CH for comets
C4	740-820	Two gaps with little OH, but one group of OH lines at 772-807nm

* Available as of January 2016

1 - SN1

Science goals :
* mostly for [OII] 3727 up to v = 10300 km/s or z=0.034
* Lyα at z=1.98 → 2.17

$\lambda_{1\%}$=361.6 nm & 386.7 nm (used to determine folding order)
$\lambda_{90\%}$=362.6 nm & 385.6 nm

Folding parameters:
* 366 – 412 nm (takes cos θ into account and center the folding)
* Step size : 1647 nm
* Order 8
* R = 1000 ➔ 228 steps (-50%, +100%); 190 steps (-25%, +100%)

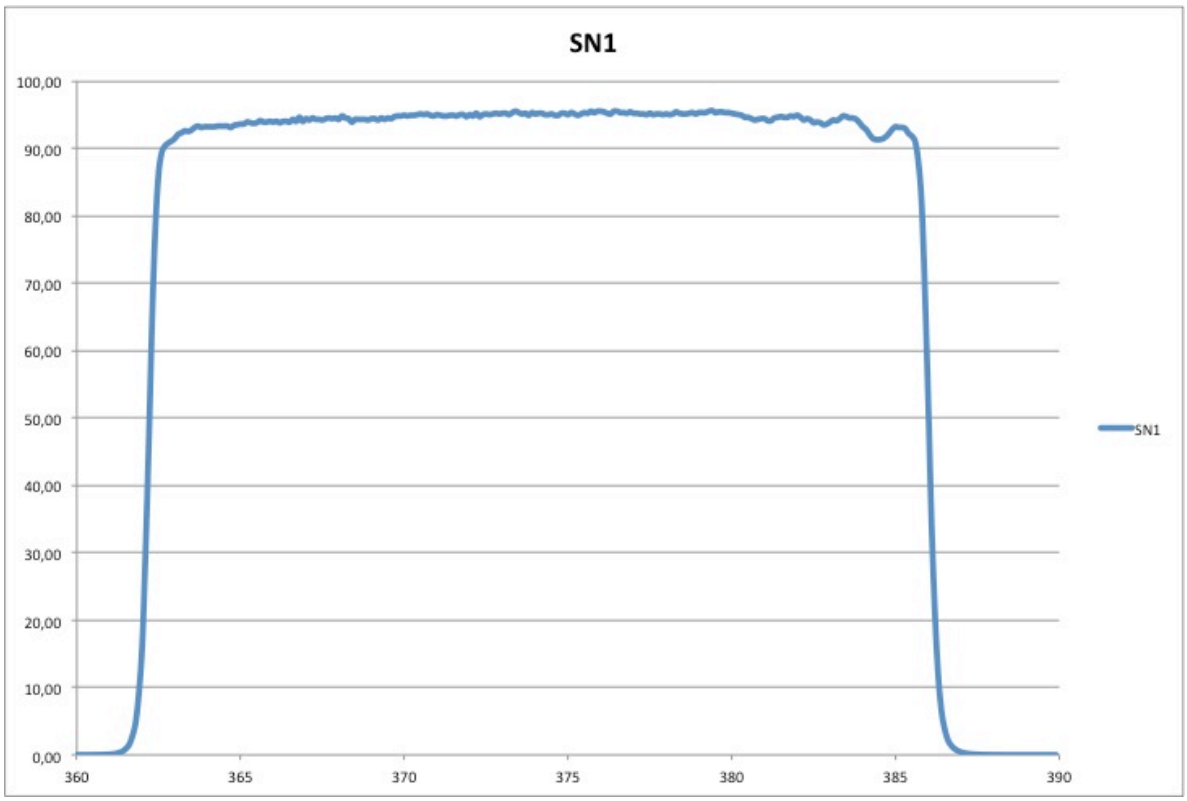

2 – C1

Science goals :

* Cosmology :
- Lyα at z=2.21 to 3.01
- [OII] 3727 at z=0.046 (14000 km/s) to z=0.29
* Galactic nebulae/nearby galaxies : Hβ (up to 1100 km/s), Hγ, Hδ, [OIII] 4363 for temperature measurement, HeII 4686 for very hot central star

$\lambda_{1\%}$=378 nm & 495 nm (used to determine folding order)
$\lambda_{90\%}$=389 nm & 484 nm

Folding parameters:

* 380 – 570 nm (takes cos θ into account and center the folding)
* Step size : 570 nm
* Order 2
* R = 500 ➔ 420 steps (-50%, +100%); 350 steps (-25%, +100%)

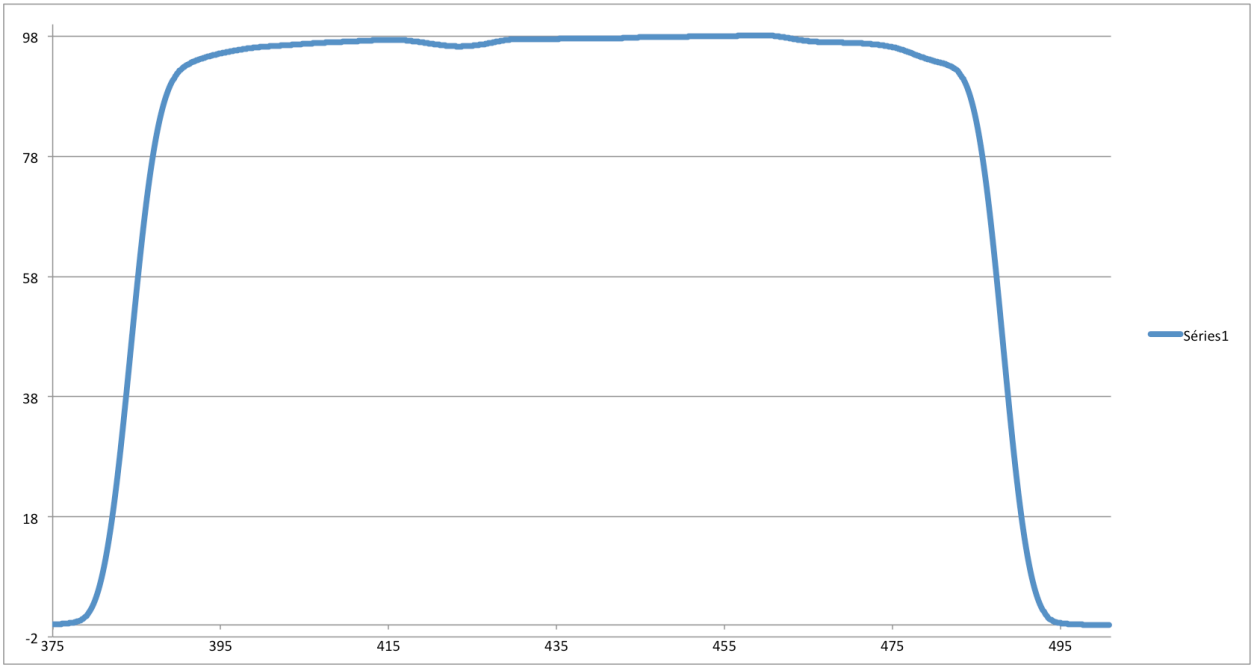

3 – SN2

Science goals :

* Galactic nebulae & galaxies: Hβ, [OIII] 4959, 5007 up to z=0.025 (7500 km/s)
* Cosmology :
- Lyα at z=2.94 to 3.23
- [OII] 3727 at z=0.29 to 0.38

$\lambda_{1\%}$=473 nm & 522 nm (used to determine folding order)

$\lambda_{90\%}$=482 nm & 513 nm

Folding parameters:

* 480 – 560 nm (takes cos θ into account and center the folding)
* Step size : 1680 nm
* Order 6
* R = 1000 ➔ 300 steps (-50%, +100%); 250 steps (-25%, +100%)

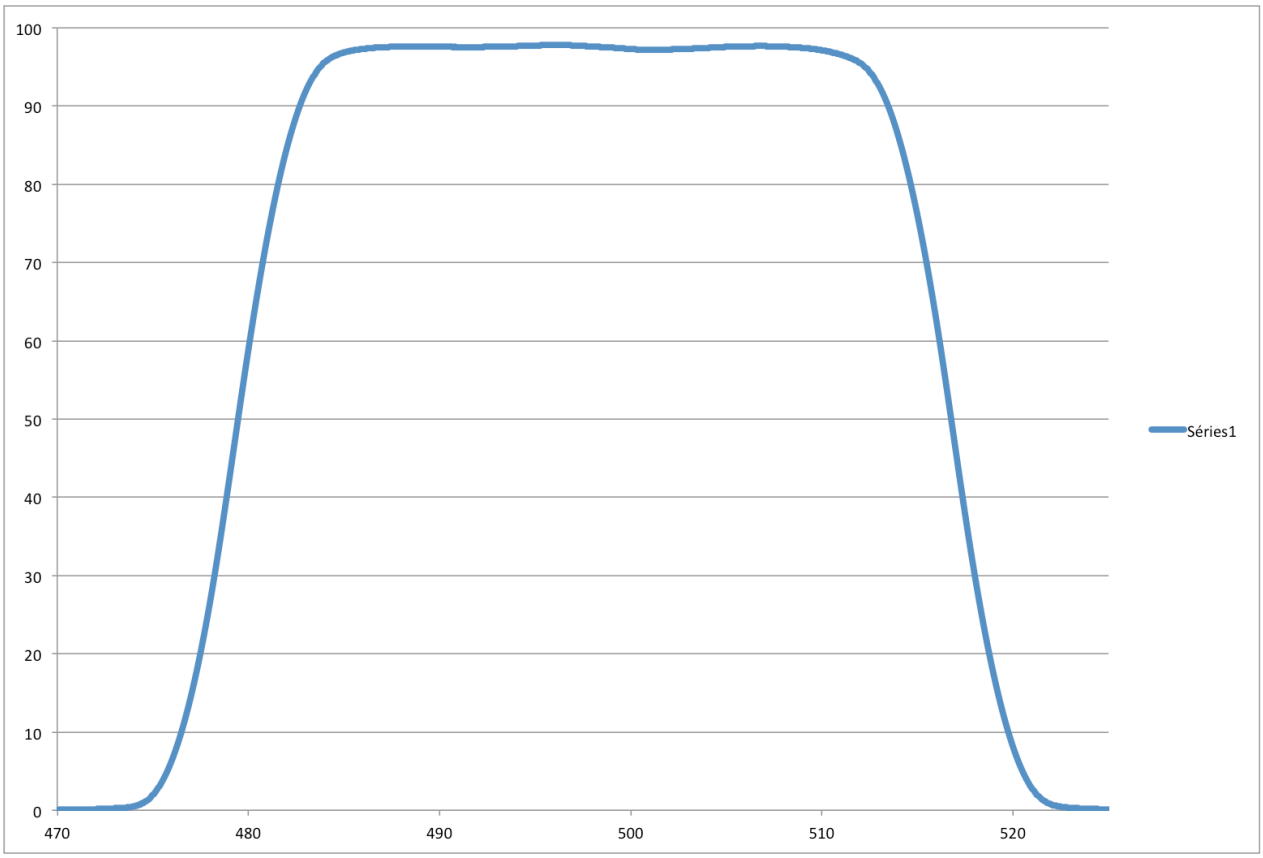

4 – C2

Science goals :

* Between sky lines ([OI] 5577 and 6300) for cosmology
* Lyα at z=3.60 to 4.14
* [OII] 3727 at z=0.50 to 0.68
* Galactic nebulae : NII 5755 for direct temperature measurement , HeI 5876

$\lambda_{1\%}$=557.9 nm & 628.2 nm (used to determine folding order)

$\lambda_{90\%}$=559.3 nm & 625.5 nm

Folding parameters:

* 560 – 672 nm (takes cos θ into account and center the folding)
* Step size : 1680 nm
* Order 5
* R = 1000 ➔ 360 steps (-50%, +100%); 300 steps (-25%, +100%)

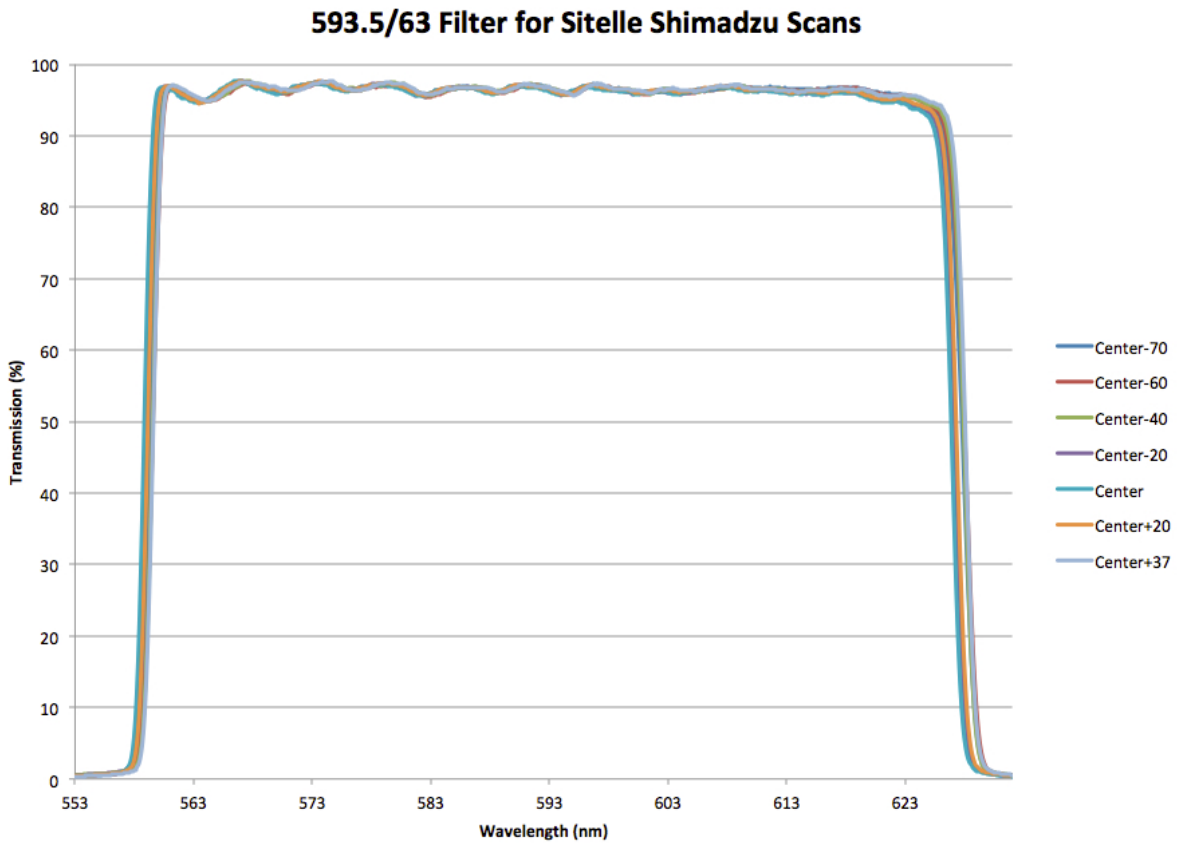

5 – SN3

Science goals :

* [NII] 6548,84, Hα, HeI 6678, [SII] 6717,31 for galactic nebulae
* Same for nearby galaxies up to v = 5400 km/s;
* [NII] 6548,84, Hα up to 12000 km/s

Cosmology :

- Lyα at z=4.32 → 4.63 (beware of OH lines!)
- [OII] at z=0.74 → 0.83

$\lambda_{1\%}$=641.6 nm & 692.8 nm (used to determine folding order)

$\lambda_{90\%}$=647.3 nm & 685.4 nm

Folding parameters:

* 654 – 736 nm (takes cos θ into account and center the folding)
* Step size : 2943 nm
* Order 8
* R = 1500 ➔ 346 steps (-50%, +100%); 289 (-25%, +100%)

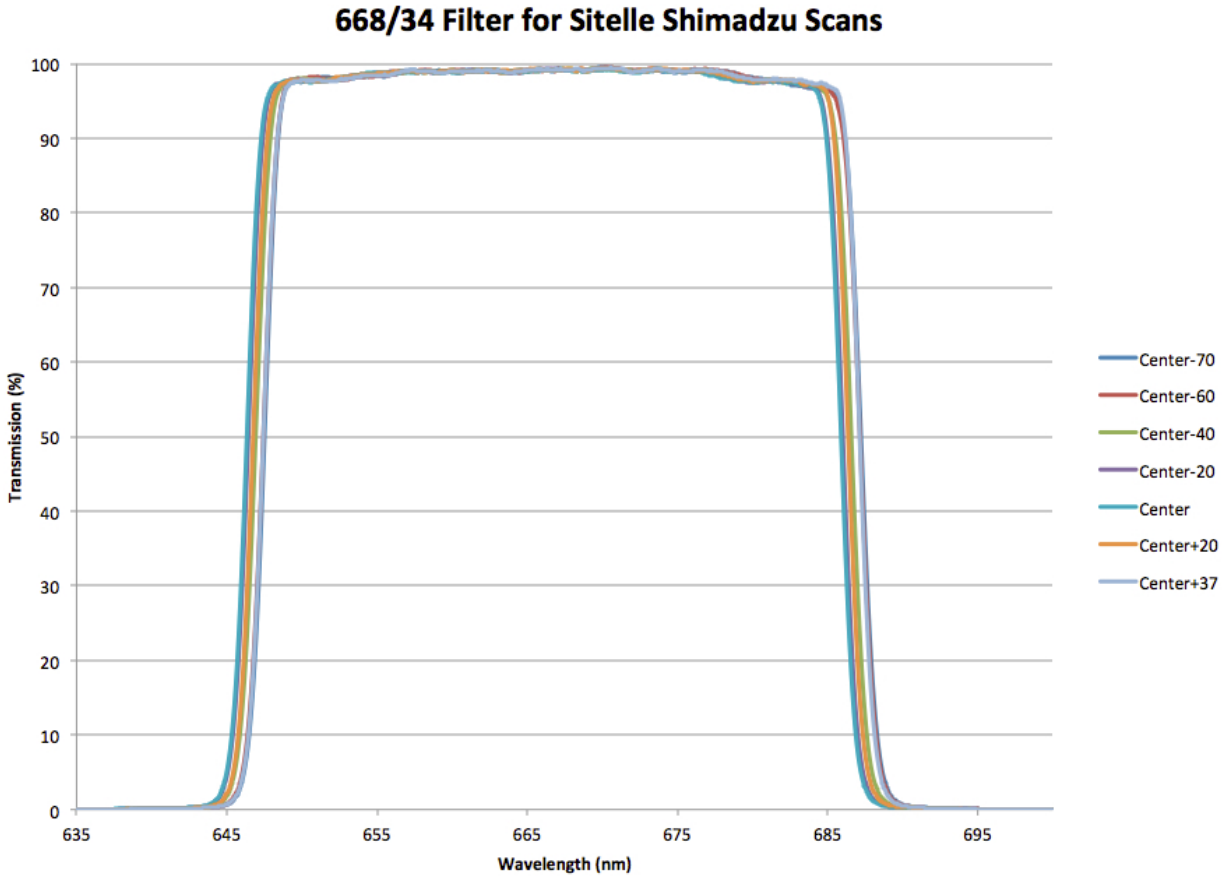

Appendix D – Modulation efficiency

This efficiency depends on a multitude of factors, the most important being the following:

1. The capability of the beamsplitter to separate the incident beam into two beams of equal intensity over the whole wavelength range (ME ∝ 4RT, where R and T refer to the reflectance and transmission of the beamsplitter). The modulation efficiency is however relatively permissive to deviation from the 50% perfect case. For example, a 60% - 40% R-T beamsplitter can still generate modulation efficiency near 96% while a 70% - 30% one would limit the performance to 84%.This is usually not a big problem over a small wavelength range, but it becomes a challenge if the FTS covers, for example, the entire visible range (from 350 to 900 nm).
2. The surface quality of the optical components in the interferometer (mirrors and beamsplitter). At a given wavelength, ME is lowered by a decreased surface quality; as can be seen in *Figure D1 (left pannel)* it is more and more difficult to obtain a good ME as we move from the infrared to the ultraviolet (most FTS commercially available indeed work in the infrared); and the number of reflections within the interferometer plays a major role in the global ME. Mirrors with a surface quality of λ/20 (peak-to-valley) are commercially available for a reasonable price, but large λ/30 mirrors must be custom made and are therefore much more expensive. Moreover, even if the mirror substrate is of high enough quality, any error in the coating deposit or any tension caused by the mechanical parts used to maintain the mirror within the interferometer can ruin the initial surface figure and dramatically reduce the modulation efficiency, especially in the blue part of the spectral range.
3. Homogeneity of the refraction index within the interferometer cavity. Any convection or temperature inhomogeneity in one or both arms can alter the OPD and therefore lower the ME, since the velocity of light depends on the refraction index of the material in which it travels.
4. The mirror alignment. In order for the beams from the two arms to interfere properly, the two mirrors need to be very well aligned. The smallest deviation, in any direction, from the optimized angle between the two mirrors reduces the spatial coherence (interference) of the two beams as they recombine. Again, this effect is more obvious at small wavelengths. A deviation of only 1.5 microradian from perfect alignement can decrease the ME by up to 40% at 350 nm – see *Figure D1(right pannel).*
5. Stability of the OPD during an exposure. The optical distance between the two mirrors must be kept constant during an exposure at a given step. An OPD jitter with a standard deviation of 10 nm typically reduces ME by 1 to 2%. The metrology and servo system play a crucial role with regard to the last two points, since the mirrors must be aligned with a precision of less than a microradian and their distance kept constant to within a few nanometers during an exposure. As we shall see later, monitoring the distance between the two mirrors as well as their alignment many thousand times per second, and a fast correction of any deviations, are required to ensure a constant, high modulation efficiency.

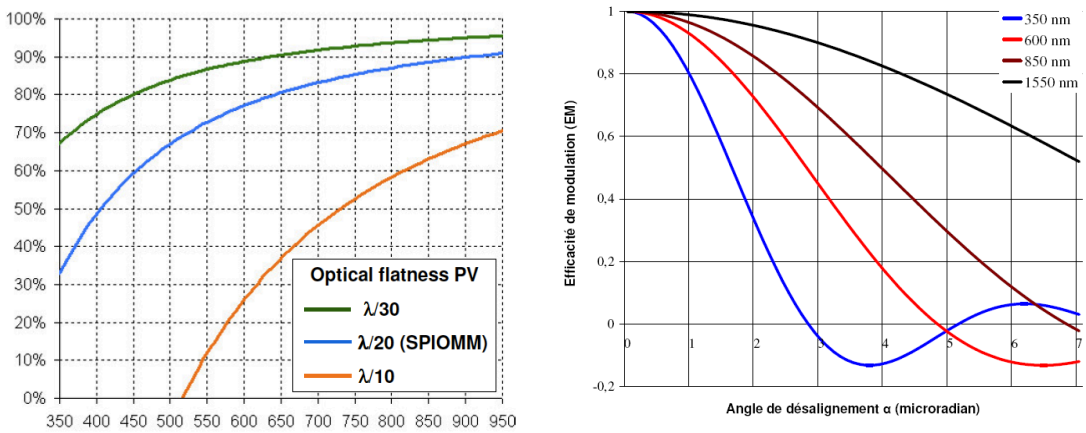

Figure D1 – Effect of the optical flatness of the mirrors/beamsplitter (left) and mirror alignment (right) on the modulation efficiency.

References

SpIOMM and SITELLE technical papers :

Brousseau, D., et al. 2014, SITELLE optical design, assembly, and testing, Proc SPIE 9147, 91473Z

Drissen, L., et al. 2014, *Imaging FTS: A Different Approach to Integral Field Spectroscopy*, Advances in Astronomy, Volume 2014 (2014), Article ID 293856

Maillard, J.-P., Drissen, L., Grandmont, F., & Thibault, S. 2013, Integral wide-field spectroscopy in astronomy: the Imaging FTS solution, Exp. Astron., Volume 35, Issue 3, pp.527-559

Martin, T., Drissen, L., & Joncas, G. 2012, ORBS : A data reduction softwre for the iFTS SpIOMM and SITELLE, Proceedings of the SPIE, Volume 8451, article id. 84513K

Drissen, L., et al. 2012, New scientific results with SpIOMM: a testbed for CFHT's imaging Fourier transform spectrometer SITELLE, Proceedings of the SPIE, Volume 8446, article id. 84463S

Grandmont, F., Drissen, L., Mandar, J., Thibault, S., & Baril, M. 2012, Final design of SITELLE: a wide-field imaging Fourier transform spectrometer for the Canada-France-Hawaii Telescope, Proceedings of the SPIE, Volume 8446, article id. 84460U

Drissen, L., et al. 2010, SITELLE: a wide-field imaging Fourier transform spectrometer for the Canada-France-Hawaii Telescope, Proceedings of the SPIE, Volume 7735, id. 77350B

SpIOMM science papers :

Lagrois, D., et al. 2015, *An optical investigation of the Dumbbell planetary nebula (M27, NGC 6583)*, MNRAS, 448, 1584

Rousseau-Nepton, L., et al. 2015, *Spiral galaxies in 3D as seen with SpIOMM*, IAU Symposium 309, p. 340.

Alarie, A., Bilodeau, A., & Drissen, L. 2014, *A hyperspectral view of Cassiopeia A*, MNRAS, 441, 2996.

Lagrois, D., Joncas, G., & Drissen, L. 2012, Diagnostic line ratios in the IC 1805 optical gas complex, MNRAS, 420, 2280

Charlebois, M., Drissen, L., Bernier, A.-P., Grandmont, F., & Binette, L. 2009, A Hyperspectral View of the Crab Nebula, AJ, 139, 2083